Volcanic emission and seismic tremor at Santiaguito, Guatemala: New insights from long-term seismic, infrasound and thermal measurements in 2018-2020

Authors:
Ellen Gottschämmer(1), Alicia Rohnacher(1), William Carter(2), Amelie Nüsse(1), Konstantin Drach(1), Silvio De Angelis(2), Yan Lavallée(2), Jackie E. Kendrick(2,3), Amilcar Roca(4), Pablo Castellanos(4), Gustavo Chigna(4), Andreas Rietbrock(1)

1. Geophysical Institute, Karlsruhe Institute of Technology, Hertzstr. 16, 76187 Karlsruhe, Germany
2. Department of Earth, Ocean and Ecological Sciences, University of Liverpool, 4 Brownlow Street, Liverpool, L69 3GP, United Kingdom
3. (Now at) School of GeoSciences, University of Edinburgh, James Hutton Road, Edinburgh, EH9 3FE, United Kingdom
4. Instituto Nacional de Sismología, Vulcanología, Meteorología e Hidrología (INSIVUMEH), Guatemala City, Guatemala

Corresponding author: Ellen Gottschämmer (Ellen.Gottschaemmer@kit.edu)

Keywords: volcano-seismology, infrasound, thermal imaging, volcano tectonic earthquakes, volcanic explosions, harmonic tremor

Abstract

Long-term instrumental monitoring of open-vent volcanoes provides the necessary datasets to characterize volcanic activity and unravel its temporal changes. This is particularly important for active lava domes, which can undergo rapid transitions in behavior over the course of their eruption. Here, we analyzed seismic, acoustic infrasound and thermographic data collected between January 2018 and September 2020 to resolve volcanic processes taking place at the Santiaguito lava dome complex in Guatemala. During this period lava effusion filled the crater of the active Caliente lava dome. The extrusive activity was accompanied by small-to-moderate explosions, prolonged episodes of gas emissions, and occasional rockfalls. Automated algorithms were applied to identify seismic signals associated with different processes and to characterize the temporal evolution of activity. We identified ~70-250 tectonic events per week and detected signals associated with gas-and ash explosions occurring at a rate of ~70-100 events/week. Lava dome growth activity was accompanied by the emplacement of a lava flow along the eastern upper flank of Caliente

and seismicity possibly due to the occurrence of rockfalls. We observed episodes of harmonic tremor in seismic and acoustic data associated with sustained gas emissions, estimated to originate at shallow depths of about 500-750 m below the crater. Data indicated that both the recurrence rate of tremor (~10-50 events/week) and its duration (~40-130 minutes/week) were slightly lower and shorter between January 2019 and March 2020 than in rest of the study period, despite minor variations in explosive activity. Finally, within a period of 11 weeks, between 18 January and 4 April 2018, we found 129 volcano tectonic earthquakes; we were able to locate 10 of them at depths between 1.3 and 2.3 km, ~1.5 km southwest of Caliente. This multi-parametric study provides valuable insights into geophysical signals and associated processes at Santiaguito, helping to resolve temporal occurrence of each event type during protracted effusive-explosive activity.

1 Introduction

1.1 Formation

Santiaguito (Guatemala) is a lava dome complex forming part of the Central American Volcanic Arc, located 110 km west of Guatemala City and 11 km south of Quetzaltenango. Santiaguito consists of four volcanic domes emplaced within the collapse scar produced by the 1902 eruption at Santa Maria volcano (Harris et al., 2003; Andrews, 2014); El Brujo, El Monje and La Mitad align on an E-W fault whilst Caliente, the easternmost dome, is slightly offset (to the south) where the E-W feeder fault intersects the main, regional NE-SW Zunil fault (Escobar-Wolf et al., 2010; Bennati et al., 2011).

A lava dome eruption began in 1922 at Caliente with a first episode of dome extrusion, which ended in 1939. Eruptive activity then shifted westward with the protracted dome growth of La Mitad (1939-1949), El Monje (1949-1958) and El Brujo (1958-1986) (Rose, 1973; Harris et al., 2003; Scott, 2013). Dome growth resumed at Caliente in 1972, and since 1975 it has commonly been accompanied by 1-2 small gas-and-ash explosions per hour (Rose et al., 1976; Rose, 1987; Johnson et al., 2014). Since 1986 Caliente is the only active dome at Santiaguito (Harris et al., 2003; Bluth and Rose, 2004). Lava extrusion rates have been observed to be cyclic with a shorter (3-6 years) phase of high extrusion followed by a longer (3-11 years) phase of low extrusion rate, identified by analysis of lava flows (Rose, 1987) and satellite data (Harris et al., 2003; Ebmeier et al., 2012). At least nine cycles of lava effusion have been identified since the formation of Santiaguito (Harris et al., 2003; Rhodes et al., 2018).

1.2 Visual monitoring

Visual observations at Santiaguito are routinely conducted by two local observers from the Instituto Nacional de Sismología, Vulcanología, Meteorología e Hidrología (INSIVUMEH, Guatemala) at OVSAN (Observatorio del volcán Santiaguito), located 7.5 km south of Caliente. However, visual observations are frequently hindered by inclement weather conditions. During the dry season (November to April) the view is often clear until around noon while during the wet season the domes are rarely visible. The summit of Santa Maria offers an exceptional vantage point to observe the development of both effusive and explosive volcanic activity and dome surface dynamics, but the abundance of visitors hampers the deployment of permanent (unguarded) equipment.

1.3 Short-term instrumental monitoring

To supplement intermittent visual observations, long-term geophysical monitoring is conducted. This helps determine the level of unrest and any change in behavior, such as shifts in eruption style (effusive vs explosive), explosion intensification, surficial mass movements, quiescence, etc. Analysis and classification of these data helps decipher eruption mechanisms and assess hazards posed. Permanent monitoring networks and visual observations can be bolstered by short, intensive, multi-parametric monitoring campaigns, which provide high-resolution data to elucidate specific eruptive processes. Santiaguito volcano is a frequent host to such efforts by several international research groups, especially during the dry season in December and January (e.g., Bluth and Rose, 2004; Johnson et al., 2004; Sahetapy-Engel et al., 2008; Johnson et al., 2008; Johnson et al., 2009; Sanderson et al., 2010; Johnson et al., 2011; Jones and Johnson, 2011; Holland et al., 2011; Scharff et al., 2012; Scharff et al., 2014; Johnson et al., 2014; Lavallée et al., 2015; Lamb et al., 2019, Carter et al., 2020, Zorn et al., 2020).

Multi-parametric surveys of dome eruption and associated explosive activity at Santiaguito have contributed to the elaboration of sophisticated physical models. Bluth and Rose (2004) observed the occurrence of gas-and-ash emissions along a ring-shape in the dome surface (ring diameter was 70 m in 2002 and 120 m in 2004). They suggested a model in which incremental plug flow due to preferential shearing near the conduit boundaries produces a ring-shape fracture that localizes gas-and-ash emissions. Sahetapy-Engel et al. (2008) determined the source depths for explosions between 100 and 620 m below the vent and stated that those must be located within a 500 m thick dacite plug in the uppermost portion of the conduit. Johnson et al. (2008) described subvertical displacements of the dome surface of ~0.5 m during explosions, with deformation starting in the center of the dome surface and propagating outward at 50 m/s. Johnson et al. (2009) performed a multi-parametric investigation and analyzed tilt, seismic and infrasonic data along with visual observations,

suggesting that explosions are preceded by elevated rates of outgassing. They also described the occurrence of multiple bursts during a given explosive event. Sanderson et al. (2010) observed ultra-long period (> 30 s) seismic signals coincident with eruptive activity centered on the active Caliente vent, which they modelled using a Mogi source located 200 m west of, and 250 m beneath the center of the vent. Holland et al. (2011) ascribed the occurrence of explosions to sudden decompression of stored gas, triggered by upward stick-slip motion of the magma plug. Scharff et al. (2014) analyzed Doppler radar images and observed that explosive events developed through multiple pulses over a 3 s period. To explain this pulsatory character, they suggested a model consisting of a magma-column containing bubble-bearing magma below a dense carapace (or plug), a few tens of meters thick. In their view, upon ascent of bubbly magma, the overlying carapace uplifts and deforms to the point of rupture or until fractures reactivate, permitting gas-and-ash emissions. They used this model to explain the fact that outgassing commonly initiates at the center of the dome. As the fractures propagate laterally across the dome, other regions of the bubbly magma fragment, leading to subsequent explosion pulses. At some point, the carapace settles back down, compressing the underlying magma once again, which may start to repressurize and initiate a second cycle of upward motion. Part of the challenge in understanding the cause for fragmentation is that the erupted lava is commonly blocky with low vesicularity (<32%), as indicated by detailed textural mapping (Rhodes et al., 2018); so fragmentation would require large pore overpressure (*cf*. Spieler et al., 2004) which is not fully consistent with the observation that the dome's integrity is largely unaffected by the explosions, and that they develop along faults, which are likely involved in the trigger source process.

Lavallée et al. (2015) combined petrological, geological and geophysical observations acquired during a week-long multiparametric survey in 2012 and reconciled observations from previous studies to expand on our model of gas-and-ash explosions at Santiaguito. Tilt data shows a regularity in inflation-deflation tilt cycles over a 25 min period (Johnson et al., 2014); this cyclicity may be driven by pulsatory gas fluxes permeating through the magmatic column (e.g., Michaut et al., 2013). The data shows that the most pronounced inflation cycles lead to gas-and-ash explosions, whereas less pronounced ones simply result in gas emission (Lavallée et al., 2015). Upon explosion, the dome surface undergoes rapid uplift/ subsidence motions of ~0.5 m in 1 s (Johnson et al., 2008) and the subsidence phase is accompanied by long-period seismicity. Magma shearing during plug flow promotes traction that generates tilt and rupture would generate the seismicity. The erupted volcanic ash contains evidence for thermal input preceding fragmentation (both melting and thermal vesiculation), which suggests that conversion of mechanical work to cataclasis and frictional

heat during fault slip may contribute to the development of volcanic ash clouds; a model which may explain the fragmentation of dense lavas, whilst ensuring localization along faults. Hornby et al. (2019a) investigated the rupture of Santiaguito lava under tensional conditions and suggested that the contrasting rates associated with the inflation phase would result in variably localized or pervasive fracture: higher strain rates during more pronounced tilt phases would promote localized fracture, whereas lower strain rates would promote more pervasive tearing of magma, thus enhancing the permeability of the system to allow outgassing (e.g., Lavallée et al., 2013). This distinction may be important as following gas or gas-and-ash emissions, depressurization of the system is accompanied by ~20 min long deflation cycles observed in the tilt signals (Johnson et al., 2014, Lavallée et al., 2015) during which gas pressure reduction in shear zones would promote progressive closure of fractures and settling of the edifice (i.e., causing negative tilt). Thus, explosions at Santiaguito appear strongly associated with faulting dynamics.

1.4 Long-term instrumental monitoring

Recently, efforts have been made to develop long-term monitoring infrastructure to improve our knowledge of prolonged eruptive behavior at Santiaguito. Between November 2014 and May 2017 a first long-term seismo-acoustic network was deployed by the University of Liverpool (De Angelis et al., 2016; Lamb et al., 2019; Carter et al., 2020; Wallace et al., 2020). Lamb et al. (2019) identified signals associated with different types of volcanic activity during this period, including explosions (of variable sizes), pyroclastic density currents, lahars and rockfalls. Their analysis revealed a shift in eruptive behavior from low-level effusion accompanied by regular, small explosions in 2014, which they refer to as the background activity level, to a highly explosive eruptive regime in late 2015 and 2016, before returning to a background level of activity in late 2016. During 2015, explosion numbers gradually reduced and by late 2015 explosions were less regular and more energetic, averaging <10 per day; in April and May 2016 the activity reached maximum intensity with several large explosions, three of them with seismic energies larger than 1 GJ, excavating a ~300 m wide, ~175 m deep summit crater in the Caliente dome (Wallace et al., 2020). The explosive phase included ejection of 2-3 m diameter ballistic bombs up to 3 km away from the vent, plumes rising up to 7 km altitude, ash fall at over 30 km distance and several pyroclastic density flows (Global Volcanism Program, 2016); in October 2016, lava extrusions began to refill the summit crater, and the explosion recurrence rate and explosion seismic energy rate returned to similar levels to 2014 (Lamb et al., 2019; Carter et al., 2020).

Despite this expanding description of volcanic unrest at Santiaguito, little is known of tremor activities, as recent studies analyzed the vertical component of seismic data only, and did not account for tremor signals (e.g., Lamb et al., 2019), which provide crucial information about magmatic fluid activity at open vent volcanoes. Volcanic tremor signals are commonly observed at volcanoes worldwide (e.g., Aki et al., 1977; Schlindwein et al., 1995; Benoit and McNutt, 1997; Konstantinou and Schlindwein, 2002; Jellinek and Bercovici, 2011; Nadeau et al., 2011). Volcanic tremor signals are characterized by signal durations of minutes to days. In some cases, frequency analysis reveals a single-frequency sine-wave or a fundamental frequency (f_0) with a set of harmonics. In those cases, the signal is described as a harmonic tremor signal (e.g., Hellweg, 2000; Lesage et al., 2006; Hotovec et al., 2013; McNutt and Roman, 2015). The generation of volcanic tremor signals is often attributed to fluid flow within the volcanic edifice and corresponding gas emissions (e.g., Seidl et al., 1981; Ripepe, 1996; Ripepe et al., 1996; Hellweg, 2000). At Santiaguito an evaluation of the occurrence of tremor in recent years has been lacking. Johnson et al. (2009) reported pre-eruptive harmonic tremor in both infrasound and seismic data for an event on 4 January, 2009. They noted different onset times prior to an explosion for the infrasound harmonic tremor signal (128 s prior to eruption) and the seismic harmonic tremor signal (125 s before the eruption), which lasted at least two minutes, with a fundamental frequency of 0.43 Hz in both and approximately 10 well-defined harmonics, which they used to infer shallow fluid flow.

Here we present new instrumental observations from the time period January 2018 to September 2020 based on a recent upgrade of our newly deployed real-time seismo-acoustic monitoring network together with new continuous thermal imagery to highlight the diversity of Santiaguito's seismic signatures and provide a comparison to previously reported activity. In particular we present some of the first analyses of harmonic tremor signals at Santiaguito to assess the potential relationships with explosive events.

2 Instrumentation

2.1 Seismic and infrasound network

Since January 2018, a collaboration between the University of Liverpool (UK), the Karlsruhe Institute of Technology (Germany) and INSIVUMEH (Guatemala) led to the deployment and operation of a new real-time seismic and infrasonic monitoring network consisting of three Nanometrics Trillium compact three-component broadband seismometers (T = 120 s) as well as one Lennartz LE3D-lite three-component seismometer (T = 1 s), three iTem prs100 infrasound sensors (Delle Donne and Ripepe, 2012) and, since 2019, an IST 2018

infrasound sensor. We carefully selected the station locations based on the previous monitoring campaigns by the University of Liverpool, to provide the best signal to noise ratio and azimuthal coverage. [Note that during the 2014-2017 campaign, five Nanometrics Trillium Compact (T = 120 s) three-component broadband seismic instruments, six Lennartz LE-3Dlite (T = 1 s) three-component short-period seismic instruments and five iTem prs100 infrasonic sensors were installed at Santiaguito volcano. During this period, the network configuration changed a few times for optimization and due to instrument failures/ repair; the locations of these stations are shown and described in Lamb et al. (2019).] The instruments of our new collaborative deployment are distributed across a network of four seismic and infrasonic stations (STG1, STG2, STG5, and STG8) at distances between 2.2 km (STG8) and 7.5 km (STG5) from the summit of Caliente (Figure 1a) occupying the positions of former stations LS07, LS08, LB06 and LB03, respectively, described by Lamb et al. (2019).

During 5-18 January 2019, we deployed an additional temporary seismic and infrasound network consisting of three Lennartz LE3D-lite three-component seismometers (stations LIN1-LIN3). The stations were located at distances between 500 m and 4 km from Caliente in order to analyze signal amplitude decay with distance (Figure 1a; Table 1). Station LIN2 was also equipped with an IST 2018 infrasound sensor.

Instrumentation for all stations in our network is summarized in Table 1. The network records continuously with a sampling frequency of 100 Hz (75 Hz at station STG2 since January 2019). Seismic data from the real-time stations are collected using a 3G modem giving a real-time understanding of current activity at Santiaguito, and allowing us to check data quality, power shortages or data loss. All infrasound and additional seismic data are collected during regular instrument service visits.

Data recovery at station STG8 amounts to 85%, 81% and 81% in 2018, 2019 and 2020 (until September), respectively.

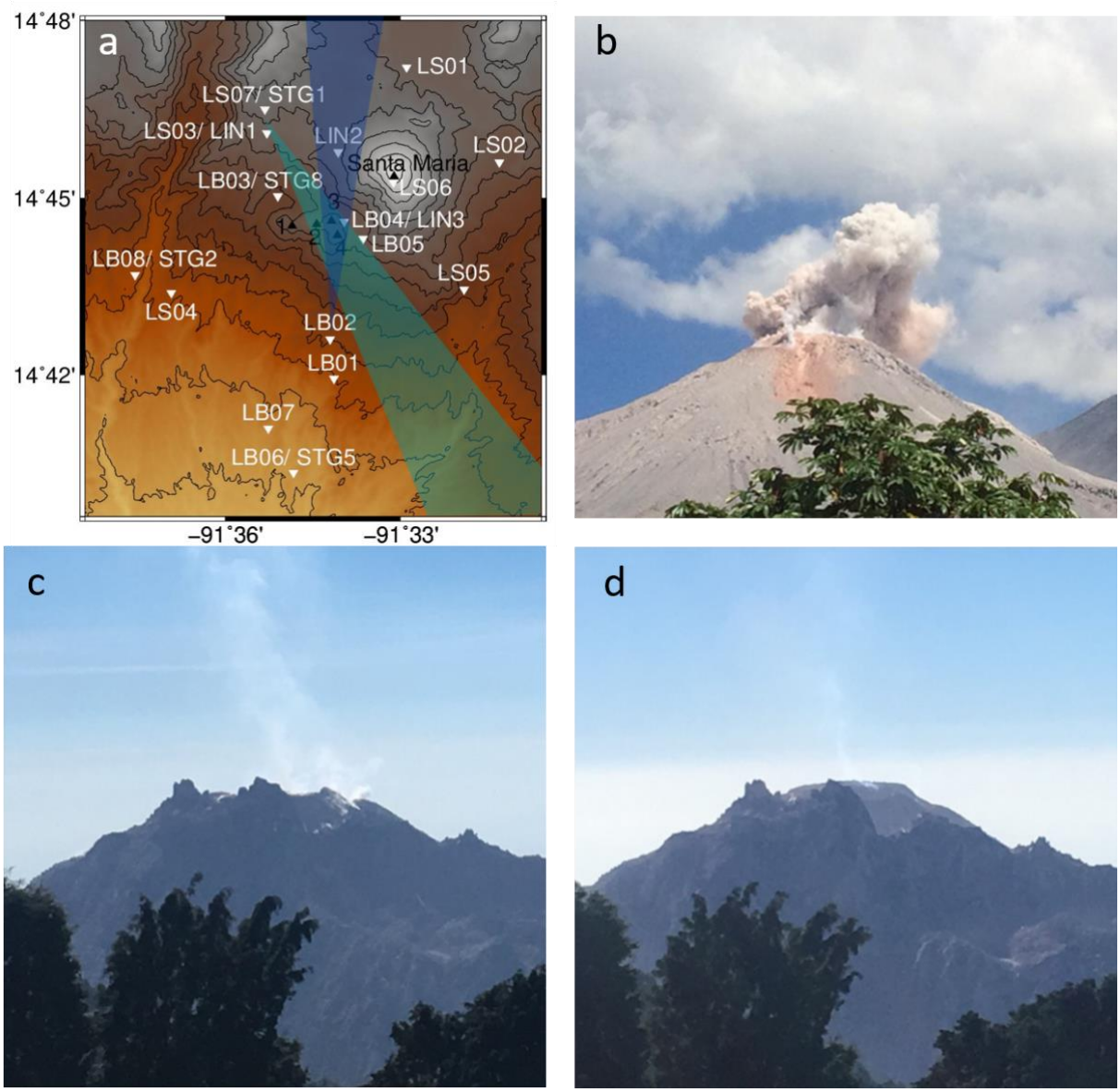

Figure 1. (a) Map of station locations around Santa Maria - Santiaguito volcanic complex. Stations STG1, STG2, STG5 and STG8 were deployed in January 2018 and operated since then. Station LIN1, LIN2 and LIN3 were temporarily installed for approximately two weeks in January 2019. Instrumentation for STG and LIN stations are listed in Table 1. LS and LB stations, which were deployed between November 2014 and May 2017 by the University of Liverpool are shown as well. Instrumentation for LS and LB stations are detailed in Lamb et al. (2019). Black triangles mark the four domes of Santiaguito, namely 1) El Brujo, 2) El Monje, 3) La Mitad and 4) Caliente. (b) Photograph of Caliente's southern flank taken 3.1 km away from LB02 on 16 January 2019, 17:16 UTC from 14.711 N/ 91.570 W. The photograph orientation is marked on panel (a) by the green region. A thin reddish veneer is visible on the southern flank of Caliente after a rockfall during the night before. (c-d) Photographs of the northwestern flank of Caliente dome taken 4.2 km away from LS03 on (c) 7 January 2018 and (d) 5 January 2019 from 14.771 N/ 91.588 W. The photograph orientation is marked on panel (a) by a blue region. The images reveal the extent of dome growth over one year.

Station name	Location (Lat/ Lon)	Distance to Caliente crater	Seismic sensor type	Deployment time seismic sensor	Infrasound sensor type	Deployment time infrasound sensor	Location of seismic installation
STG1	14.77/ -91.59	4.5 km	LE3D	07/01/2018	IST2018	18/01/2019	On a splint inside a small house.
STG2	14.73/ -91.63	6.3 km	TC120	06/01/2018	iTem prs100	06/01/2018	On a splint inside a small house.
STG5	14.67/ -91.58	7.5 km	LE3D TC120	06/01/2018 10/05/2018	iTem prs100 IST2008	06/01/2018 07/01/2019	Within plastic barrel with concrete foundation.
STG8 (known as VIP camp)	14.75/ -91.59	2.2 km	TC120	08/01/2018	iTem prs100	08/01/2018	Within plastic barrel with concrete foundation.
LIN1	14.77/ -91.59	3.9 km	LE3D	05/01/2019	No sensor	-	Seismic sensor buried.
LIN2	14.76/ -91.57	2.6 km	LE3D	05/01/2019	IST2018	05/01/2019	Seismic sensor buried.
LIN3	14.74/ -91.56	0.5 km	LE3D	06/01/2019	No sensor	-	Seismic sensor buried.

Table 1. Location and instrumentation of seismic and infrasound stations. Stations STG1, STG2, STG5 and STG8 belong to latest long-term deployment since January 2018, stations LIN1, LIN2 and LIN3 are part of temporary network in January 2019. Station locations are mapped in Figure 1a.

2.2 Thermographic camera

In January 2019, we installed an AXIS Q-1942E thermographic camera at OVSAN (co-located with STG5), which is directed northward to resolve proximal activity. With a viewing angle of 10° the camera captures the southern portion of Caliente and its emissions up to approximately 500 m above the vent. The thermographic images are recorded every second at a resolution of 640 x 480 pixels, corresponding to an approximate horizontal resolution of 2 m/pixel at the summit vent. Of these, one image per minute is transmitted in real-time and the images recorded every second are stored until collection. The images enable continuous characterization of thermal fluctuations arising from, for instance, gas and ash emissions or rock falls, during both day and night in clear conditions. Visual observations made in January and May 2018, as well as in January 2019, complete our survey.

3 Methods

This study of the January 2018 – September 2020 activity at Santiaguito focuses primarily on the seismic signals associated with ongoing eruptive activity and calls upon infrasound, visual and thermographic data to complement analysis and constrain processes when possible. Our network has captured seismic events with different signatures, which we quantify and analyze to characterize long-term seismicity at Santiaguito.

First, a catalogue of seismic events with impulsive onset was created by analyzing for average amplitude ratio in short to long time windows (STA/LTA), following previous efforts at Santiaguito (e.g., Lamb et al., 2019; Carter et al., 2020, for more details on the method see section 3.1). To discriminate between the origin of signals (e.g., from explosions vs fault-related earthquakes), in a second step we used an algorithm based on averaged amplitude spectra computed for explosion and earthquake signals (section 3.2) resulting in two separate catalogs (an explosion catalog and an earthquake catalog). Finally, automated search algorithms were applied to the earthquake catalog in order to detect volcano tectonic (VT) earthquakes with low s-p arrival delay compared to distal tectonic events (sections 3.3 and 3.4). Tremor signals were detected in a separate analysis making use of spectral properties of the tremor signal (section 3.5). Finally, a tremor source depth estimation was performed (section 3.6).

3.1 Catalog of seismic events by STA/LTA analysis

An automated moving-window analysis was performed, and averaged amplitudes were computed for short-term windows of 1 second and long-term-windows of 75 s. In cases where the STA/LTA ratio exceeded a threshold value of 6 the signal was regarded as an impulsive signal. The end of the signal was determined by an STA/LTA threshold value of 1.2 or below. The signal was added to the catalog only in the event that the threshold was exceeded on all three components of station STG8 and three components of any other seismic station at the same time.

3.2 Determination of explosion and earthquake seismic signals

To discriminate between explosion and earthquake seismic signals, we manually inspected the waveforms and amplitude spectra of the events catalogued during 18-24 January and 19-20 February, 2018, and complemented our discrimination of events by analysis of infrasound data and thermographic imagery associated with the generation of volcanic plumes during explosions. During these periods, 60 explosions and 107 earthquakes were identified; these

events were then subjected to waveform analysis to constrain average amplitude spectra of explosions and earthquakes to use as a template in subsequent automated detection efforts to construct two separate catalogs of explosions and of earthquakes. Events were classified provided that their signals fell within one standard deviation of the average template spectra.

3.3 Automated volcano tectonic (VT) earthquake search by cross-correlation

To identify the VT earthquakes from our earthquake dataset we computed cross-correlations, using two template events (10/03/2018 UTC 19:18 and 26/03/2018 00:23 UTC). We selected these templates by visual inspection of the data at station STG8, as this proximal location (2.2 km away from Caliente) provides the best signal quality (in our network) and has been frequently used as a monitoring site in previous campaigns (Lamb et al., 2019; Carter et al., 2020). The search for VTs was then conducted via automated cross-correlation of the two template events with a length of 30 s, which we filtered between 1 – 8 Hz, the dominant frequencies of such events at Santiaguito. We determined the correlation coefficient between the templates and seismic records of 30 s, for three months between January and April 2018, and classified signals as VTs when they showed a correlation coefficient of ≥0.8. This criterion is stricter than the minimum cross correlation coefficient threshold of 0.7 commonly stipulated in previous studies (e.g., Green and Neuberg, 2006; Salvage and Neuberg, 2016). Furthermore, we imposed that an event must be recorded at two stations, or more, to qualify as a VT, with the earliest record appearing at station STG8, which is closest to Caliente.

3.4 Volcano tectonic earthquake hypocenter analysis

The hypocenters of volcano tectonic earthquakes were determined by triangulation using the P- and S-wave onsets' arrival time difference (Δt) and by considering nominal P- and S-wave velocities (V_p and V_s, respectively). We inverted simultaneously for hypocentral parameters and V_p/V_s ratio by minimizing root-mean-square (RMS) errors for arrival times.

3.5 Automated tremor detection algorithm

To identify harmonic tremor sequences from the original monitored datasets, we implemented an automated tremor detection algorithm. The harmonic signals comprise a fundamental frequency (first harmonic) at f_0 and consecutive harmonics at $f_0 + n \cdot f_0$ for integer n. Thus, the second harmonic is located at $2 \cdot f_0$, and consecutive harmonics at higher multiples of f_0.

The algorithm first computed the amplitude spectra for a certain time window. After having tested several window lengths, it showed that a time window of 36 s was most appropriate: The window length needed to be long enough to resolve the fundamental frequency f_0 and integer harmonics in the spectral domain, but short enough to avoid smearing of spectral peaks when gliding occurred. In a second step, our algorithm searched for the frequency interval between neighboring peaks in the amplitude spectra. Our method assumed that both even and odd harmonics are equally present in the waveform, which was checked manually before automatic application of the search algorithm. To assess uncertainties we computed the standard deviation of the frequency intervals for neighboring peaks in one time window. For standard deviations equal to or less than 0.1, a signal was classified as harmonic tremor, provided that this condition was met more than once when interrogating the continuous signal in sequential time windows over an interval of 100 s. A similar algorithm was proposed by Roman (2017), who opted to designate the frequency with the maximum power as fundamental frequency. Our algorithm allows the amplitude of the fundamental frequency to be lower than the amplitude of subsequent harmonics.

3.6 Automated tremor source depth determination

The source depth of tremor was estimated in order to resolve source processes associated with the volcanic activity observed. This was possible by evaluating the amplitude decay of signals as a function of distance from the volcano. From the amplitude spectra, we obtained A_N, which is the spectral amplitude A of the second harmonic at the N^{th} station, as the amplitude of the fundamental frequency, or first harmonic, was often superimposed by low-frequency noise. We performed a linear fit using the function

$$\log A_N(R_N) = \log A_0 - n \cdot \log R_N \quad (1)$$

where R_N is the hypocentral distance between the source and station N, A_0 is the signal amplitude at the source and n is the gradient of the linear regression, thus when n=1, 1/R constrains the reciprocal fall-off of amplitude with distance. This assumption is valid for body waves in a homogeneous medium neglecting attenuation, providing a first-order approximation of source depth. The hypocentral distance R_N depends on source depth z, which we varied in our analysis, and on distances X_N between the N stations and Caliente and is expressed as

$$R_N = \sqrt{X_N^2 - z^2} \quad (2)$$

for each station. This restricts the source location to the area directly below the crater of Caliente. We computed linear regressions considering depths between 0 and 8000 m and evaluated their misfit; the source depth resulting in the smallest misfit was identified as the most likely source depth for the harmonic tremor signal.

4 Observations and Analysis

The following visual descriptions of volcanic activity are based on our observations during field campaigns and monitoring work from OVSAN. During January 2018 – September 2020, the activity at Santiaguito remained centered at Caliente lava dome. It was characterized by the extrusion of blocky lava along with the emissions of gas and ash several times a day. The gas-and-ash plumes generally reached up to 600-700 m above the dome. Rockfalls and small pyroclastic density currents were also observed on the eastern flank of Caliente, and during Guatemala's rainy season, small lahars occurred down the main local tributaries. [Note that more detail is available through the 2018-2020 weekly volcanic activity reports at Santa Maria; see Global Volcanism Program website of the Smithsonian Institution.]

Between January 2018 (Figure 1c) and January 2019 (Figure 1d) we observed substantial dome growth at Caliente, clearly visible by eye from a distance of 4 km. We estimated the elevation difference at several tens of meters. During one of our campaigns on 16 January 2019, we witnessed a gas-and-ash explosion followed by a large breakoff of rocks, which triggered rockfalls along the southern flank of the dome; this activity resulted in the transport and deposition of ash at OVSAN (7.5 km away) and left an extensive exposed reddish area covering about 10^4-10^5 m^2 on the flank of Caliente (Figure 1b).

We evaluated the occurrence of characteristic signals monitored at Santiaguito to constrain volcanic activity during the study period (Figure 2). The different types of seismic signals recorded are presented and analyzed, and supplemented by acoustic infrasound and thermographic data (when available and required) to support our interpretation of the seismic observations.

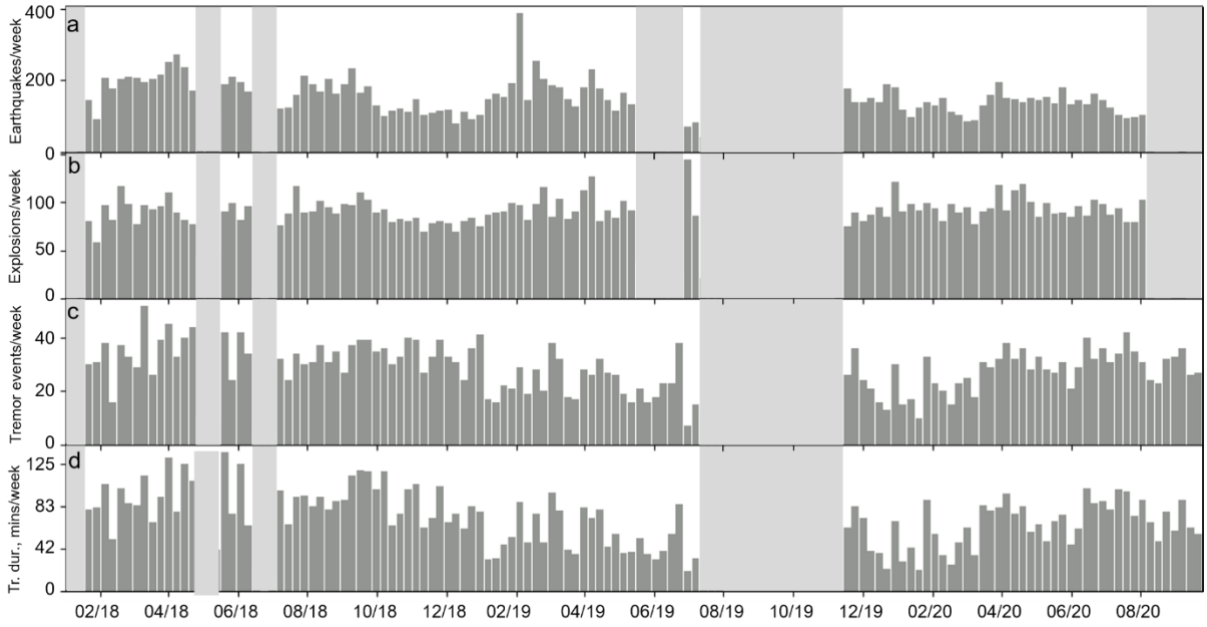

Figure 2. Classified seismic events recorded at Santiaguito in the study period January 2018 to September 2020. The light grey boxes indicate periods in which some stations were not operational which prevented identification of events: (a) Number of earthquakes per week. (b) Number of explosions per week. (c) Number of tremor events per week. (d) Tremor signal duration in minutes per week (Tr. dur., mins/week).

4.1 Regional tectonic earthquakes

The seismic network monitoring activity at Santiaguito inevitably recorded local and regional tectonic earthquakes, as the volcano is situated in the Central American Volcanic Arc, associated with active subduction of the Cocos plate under the Caribbean plate (Burbach et al., 1984). We identified tectonic earthquakes as signals with frequencies between 2 and 12 Hz, and impulsive P- and S-wave onsets with an arrival time difference of several seconds (3-20 s; Figure 3a-d). The spectrograms computed for velocity showed clear distinctions between the P and S waves, as S-wave onsets were characterized by higher amplitudes and slightly higher frequencies than the P waves (Figure 3e-h).

We identified 16,362 earthquakes during 2018-2020 (7,486 in 2018; 4,698 in 2019, and 4,178 in 2020 before 30 September, with data gaps of 53, 169 and 51 days in each year, respectively, Figure 2a); these numbers are considerably larger than those routinely catalogued by INSIVUMEH (e.g., 866 events of local magnitudes between 2.4 and 6.1 during 2018; 3640 events of local magnitude between 1.8 and 5.6, INSIVUMEH, 2019) due to different thresholding of equipment and analysis. During the study period, we identified generally between ~70 and 250 earthquake events per week, except for a brief spike of 390 events per week in February 2019, attributed to a magnitude M=6.7 event (and aftershocks)

which occurred 88 km away in southern Mexico (2019-02-01,16:14:12 UTC) and produced multiple aftershocks. Overall the dataset constrained on average 22.4 daily earthquakes between January 2018 and the end of September 2020.

A magnitude 4.1 earthquake on 14 July 2018 (06:20 UTC), located about 11 km south of Caliente, close to the village of El Nuevo Palmar, at an approximate depth of 50 km is shown in Figure 3. This earthquake displayed P- and S-wave onset arrival time difference of the order of about 10-13 s, thus providing a clear distinction to VT events with shorter arrival time differences (see section 4.2).

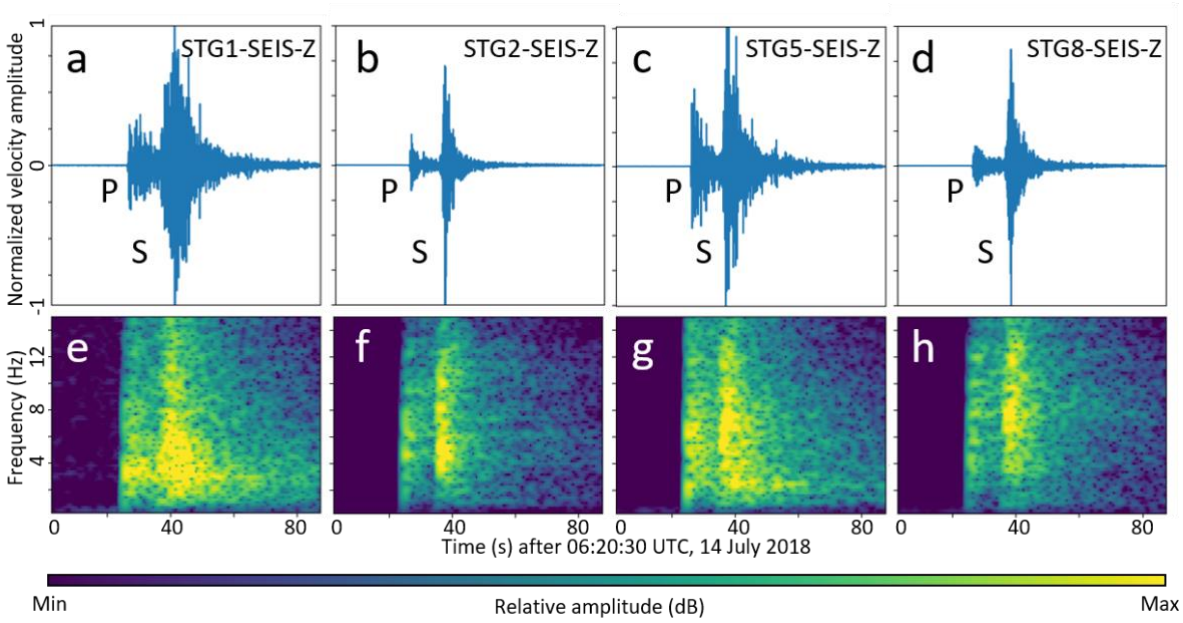

Figure 3. Tectonic earthquake recorded on 14 July 2018 (06:20 UTC). Top row: Vertical component of velocity seismograms for the four long-term stations (a) STG1, (b) STG2, (c) STG5, and (d) STG8. The seismic data were bandpass filtered between 0.3 and 15 Hz. The tectonic earthquake was located by INSIVUMEH at a distance of about 11 km south of Caliente close to the village of El Nuevo Palmar at a hypocentral depth of 50 km and was the closest tectonic event to Caliente reported by INSIVUMEH during the study period. Impulsive P- and S-waves can clearly be distinguished and are marked in the seismograms. (e-h) Spectrograms or the above seismograms. Most of the energy is found above 2 Hz for all four stations.

4.2 Volcano tectonic earthquakes

Volcano-tectonic (VT) earthquakes are events generated in the vicinity of volcanic edifices, with sharp, mostly impulsive P-wave arrivals, whilst S-wave arrivals are often difficult to distinguish because of their short travel distances (e.g., Chouet and Matoza, 2013). Between 18 January and 4 April 2018, we identified 129 VT events that met our identification requirements (i.e., recorded at two stations including STG8, with the earliest arrival at STG8).

Typical signal durations are around 30 s, and the difference in arrival times between P- and S-waves (Δt) are on the order of 0.6 s at station STG8, the closest to the crater. In a joint inversion of hypocentral parameters, V_p, and V_p/ V_s ratio, hypocenters were calculated for 10 VT events, which had been recorded at ≥ 3 stations. Hypocenters are marked as yellow stars in Figure 4. The hypocenter locations are aligned at depths between 1.3 and 2.3 km about 1.5 km south-west of Caliente. The horizontal and vertical uncertainties in the hypocenter determination amount to 100 m and 200 m, respectively. We observed no spatial migration of hypocenters with time. The inversion yields V_p of 3.85 km/s, and a V_p/ V_s ratio of 1.73. Figure 5 displays the two horizontal (NS and EW) and the vertical component of seismic data (along with its amplitude spectra) recorded on 10 March 2018 (19:18 UTC) at STG8. It can clearly be seen that the frequency content of the VTs is higher than for the case of regional tectonic activity (Figure 3); most of the energy is found between 6 and 12 Hz (Figure 5) and, like the tectonic events, the signal does not contain significant energy at frequencies below 2 Hz.

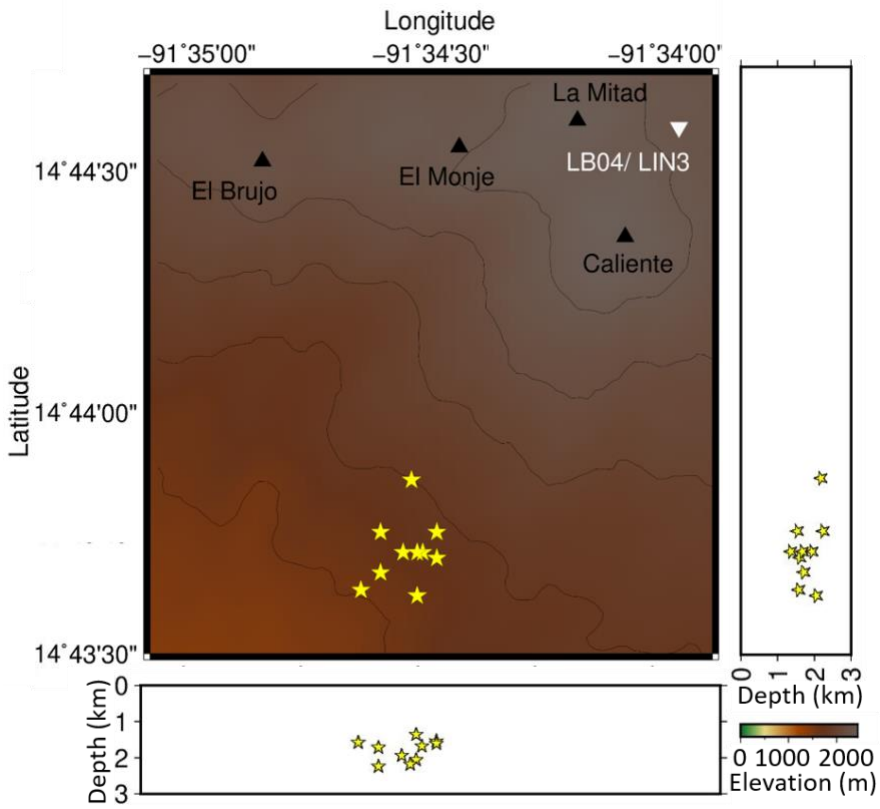

Figure 4. Location of ten volcano tectonic earthquakes recorded between 26 January and 4 April, 2018. The epicenters are indicated as yellow stars in the map. They are located closely together about 1.5 km southwest of Caliente. The cross sections show that the hypocenters for those events are located at depths between 1.3 and 2.3 km.

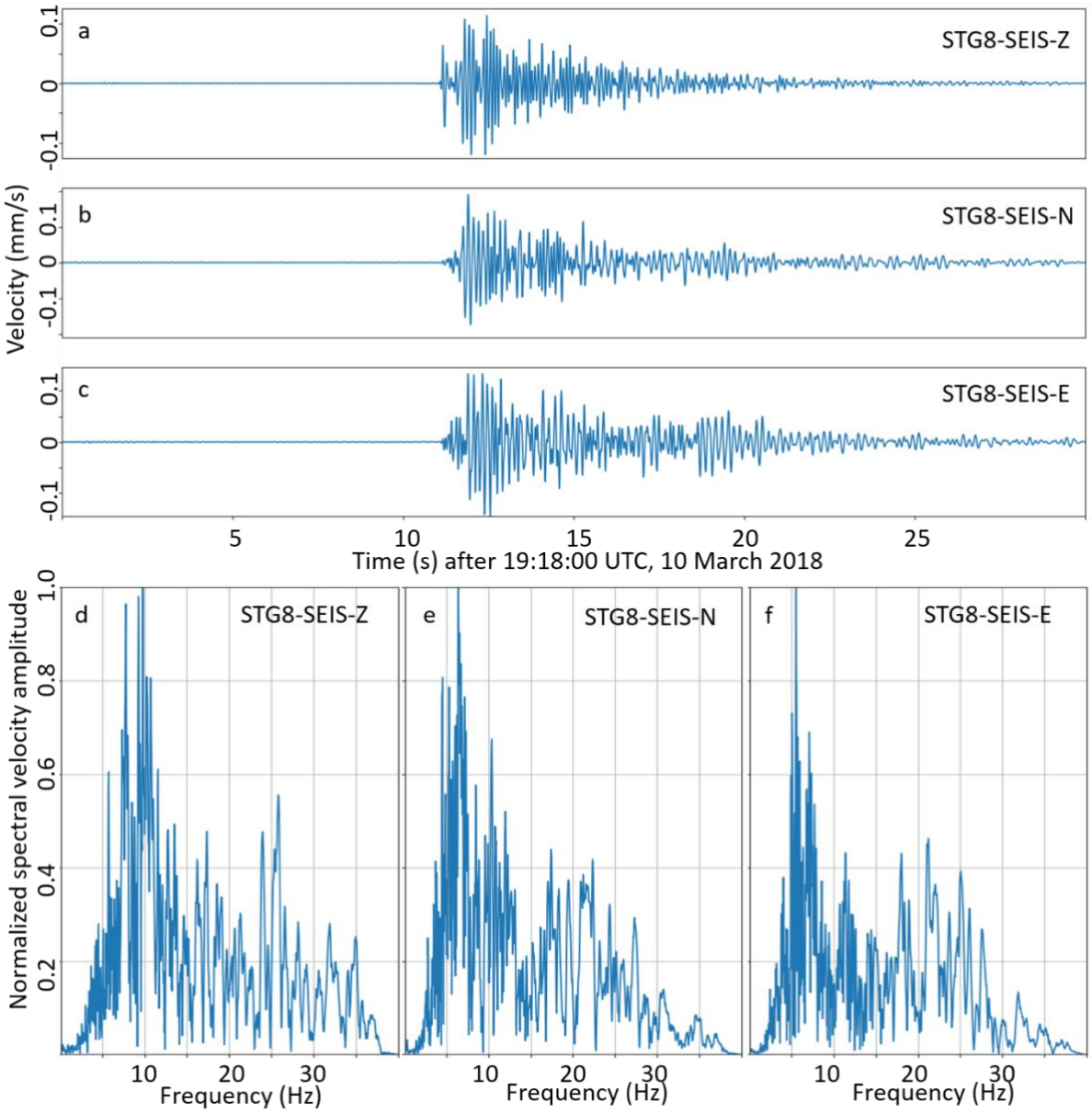

Figure 5. (a) vertical, Z, and (b-c) horizontal, N and E components respectively, of velocity seismograms for a volcano tectonic earthquake recorded at station STG8 on 10 March 2018 (19:18 UTC). The data have been bandpass filtered between 0.5 and 15 Hz. (d-f) Amplitude spectra for the three time series in a-c.

4.3 Explosion seismic signal analysis

Gas-and-ash explosions were witnessed several times per day in the study period (see Global Volcanism Program for further detail), as Santiaguito exhibiting activity comparable to non-paroxysmal periods (e.g., Carter et al., 2020) commonly described in several studies (e.g., Sahetapy-Engel et al., 2008; Johnson et al., 2009; Johnson et al., 2011; Lamb et al., 2019). These resulted in the generation of seismic and acoustic infrasound signals. Using an automated detection algorithm on the data stream (see section 3), we identified the frequent

occurrence of explosions. The signals of explosions were characterized by an impulsive onset preceded by a low-amplitude precursory signal with a duration of approximately 2-4 s (Figure 6a-c). These explosions had characteristic frequencies of 1-4 Hz and the amplitudes generally decayed rapidly to background levels within 60-90 s.

At stations where a seismometer was co-located with an acoustic infrasound sensor, the onset time of a seismic signal of the explosion was generally followed by arrival of an acoustic wave. At the closest station STG8 we observed 6.9 s of delay whereas at station STG5, located at a distance of 7.5 km from Caliente, the seismic signal arrived approximately 20 s earlier than the infrasound signal (Figures 6c and d showing the comparison for STG5). The corresponding spectrograms in Figure 6e-h suggested that the main energy of both the seismic and infrasound signals generated by these gas-and-ash explosions was primarily below 4 Hz.

Thermographic images simultaneously recorded at the location of STG5 provided invaluable visual information for correlating the seismic and infrasonic data with volcanic activity (Figure 6i). Images recorded at 12:07:20 UTC (i.e., before the seismic signal), 12:07:30 UTC, 12:07:45 UTC, and 12:08:00 UTC confirmed that the seismicity characterized by frequencies below 4 Hz corresponds to explosions from Caliente's central vent. The images also reveal that the seismic signal was short in comparison to the thermal anomaly associated with prolonged venting from the crater.

Altogether, the explosion catalog indicated the frequent occurrence of gas-and-ash explosions at Santiaguito, with on average 70-100 weekly explosions (Figure 2b). The study period shows no long-term increase or decrease in activity; instead, the data appear to show slight variations in explosion recurrence rate in ~6-month intervals.

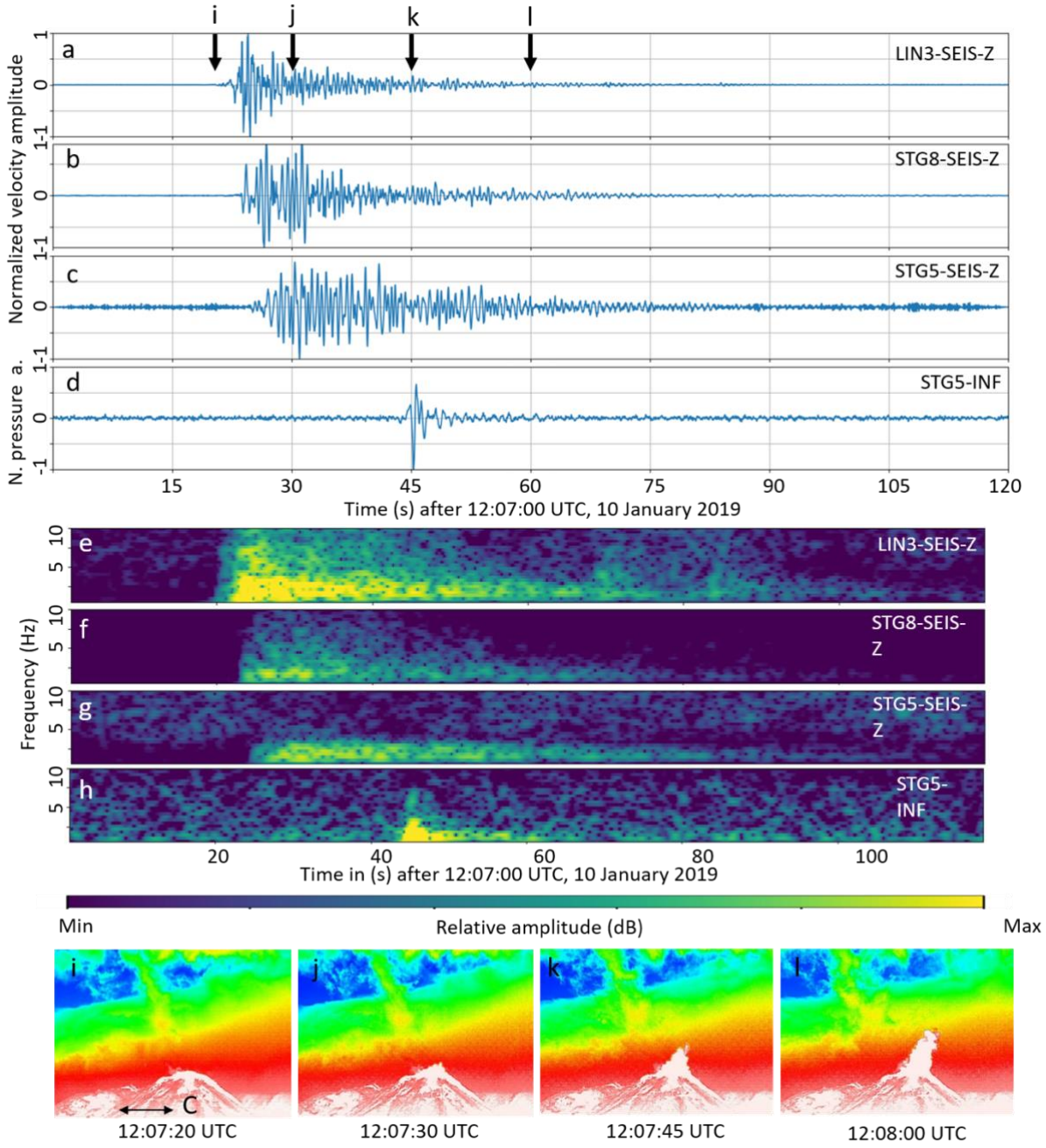

Figure 6. Normalized vertical component of velocity seismograms for stations (a) STG5 (7.5 km away from Caliente), (b) STG8 (2.2 km) and (c) LIN3 (0.5 km), and (d) normalized infrasound signal (N. pressure a.) recorded at STG5 for a central vent explosion on 10 January 2019. Data have been filtered between 0.5 Hz and 10 Hz. (e-h) Spectrograms of the corresponding seismograms above. (i-l) Thermographic images recorded viewing NNE from STG5 prior to (i) and during (j-l) the seismic signal (timing indicated on panel a). C (marked in panel i) shows Caliente. The length of the arrow in panel i) corresponds to approximately 300 m at Caliente summit. White colors indicate the relatively warm regions, blue colors indicate relatively cold regions.

4.4 Analysis of eastern flank activity

Thermographic image analysis revealed the occasional upwelling of hot plumes from the eastern flank of Caliente that we associate to the lava flow (Figure 7). The plumes are not long-lived and display a discrete appearance. Visual correlation of those episodes with the seismic signal shows that the episodes are accompanied by seismic signals with a variably emergent onset, a long duration (up to several minutes) and slowly decaying coda; yet, no acoustic signals are associated with their occurrence.

We perform a spectral analysis for the seismic signals during those episodes in order to enable their clear distinction from explosive signals (described in section 4.3). Our analysis indicated that most of the energy is located at frequencies between 2-14 Hz with a maximum energy at around 8-10 Hz; that is at higher frequencies than signals associated with explosions from the central vent. Analysis of the monitored records in the study periods indicated that flank activity occurred across the whole study period.

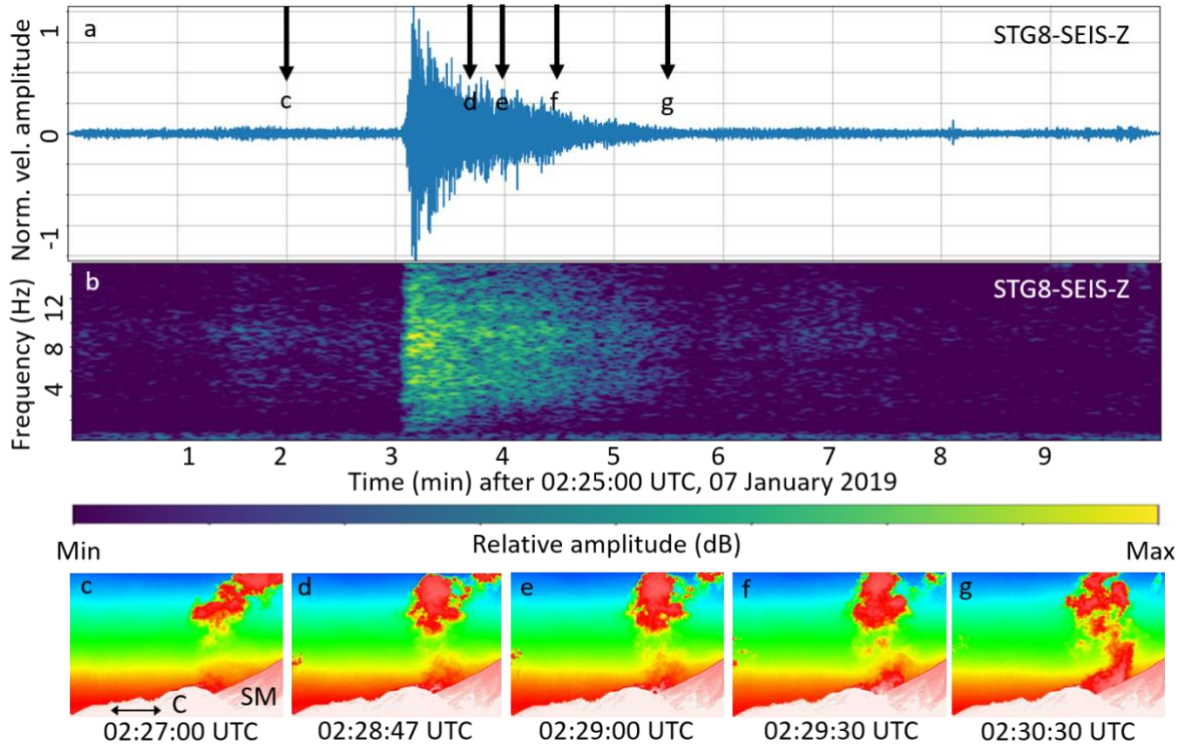

Figure 7. Signals of flank activity. (a) Vertical velocity seismogram along with (b) spectrogram recorded on 7 January 2019, between 02:25 UTC and 02:35 UTC at station STG8 (at 2.2 km from the active vent Caliente). c-g) Thermographic snapshots of persisting fumarolic flank activity prior to (c) and after the start of the seismic signal at (d-g) (marked by arrows in panel a). C and SM (in panel c) mark Caliente and Santa Maria, respectively. The length of the arrow in panel c) corresponds to approximately 300 m at Caliente summit. White colors indicate the relatively warm regions, blue colors indicate relatively cold regions.

4.5 Tremor signal analysis

Between January 2018 and September 2020, our search algorithm revealed between 10 and 50 harmonic tremor events per week in the seismic record (Figure 2c). We observed around 20, and sometimes up to 30, even and odd integer harmonics in the seismic records. The seismic tremor sometimes coincided with up to 7 faintly developed harmonics in the infrasound data (Figures 8 and 9). The length of the tremor signals varied from 100 s, which is our minimum detection threshold, up to 20 minutes. However, most of the signals had a duration of 3-4 minutes. The total duration of tremor varies between 20 and 130 minutes per week (Figure 2d). Whenever thermographic images were available (when operational and weather permitted), we observed that tremor signals coincided with the emission of hot gas (and possibly ash) clouds (Figure 10). The tremor signals were observed either directly or a few minutes after the onset of an explosion. Below, we describe the variable character of three tremor sequences to show typical occurrences and analyze their source depth as these signals have seldom been examined at Santiaguito.

4.5.1 Tremor observation

Figure 8 shows a tremor signal that occurred on 8 February 2018. The tremor signal exhibited an emergent onset; overall, the signal showed amplitude modulations and consisted of three broad bursts with increasing amplitude. The first burst was clearly distinguishable from the second burst, while the second and the third bursts seemed to overlap. The fundamental frequency f_0 observed in the spectrograms of this tremor amounted to approximately 0.5 Hz and varied slightly (Figure 7 bottom). Up to 27 evenly spaced harmonics were recorded at station STG8 while at stations STG1, STG2, and STG5, harmonics above 6 Hz were hardly visible. The first three harmonics were visible in the infrasound recording. The three bursts, which were observed in the seismic traces were also identified in the spectrograms. At the end of the first burst (around 180 s), the fundamental frequency glided up and with the start of the second burst the fundamental frequency glided down. A sudden decrease in fundamental frequency was observed upon transition from the second to the third burst around 310 s; this corresponded to a sudden increase in amplitude.

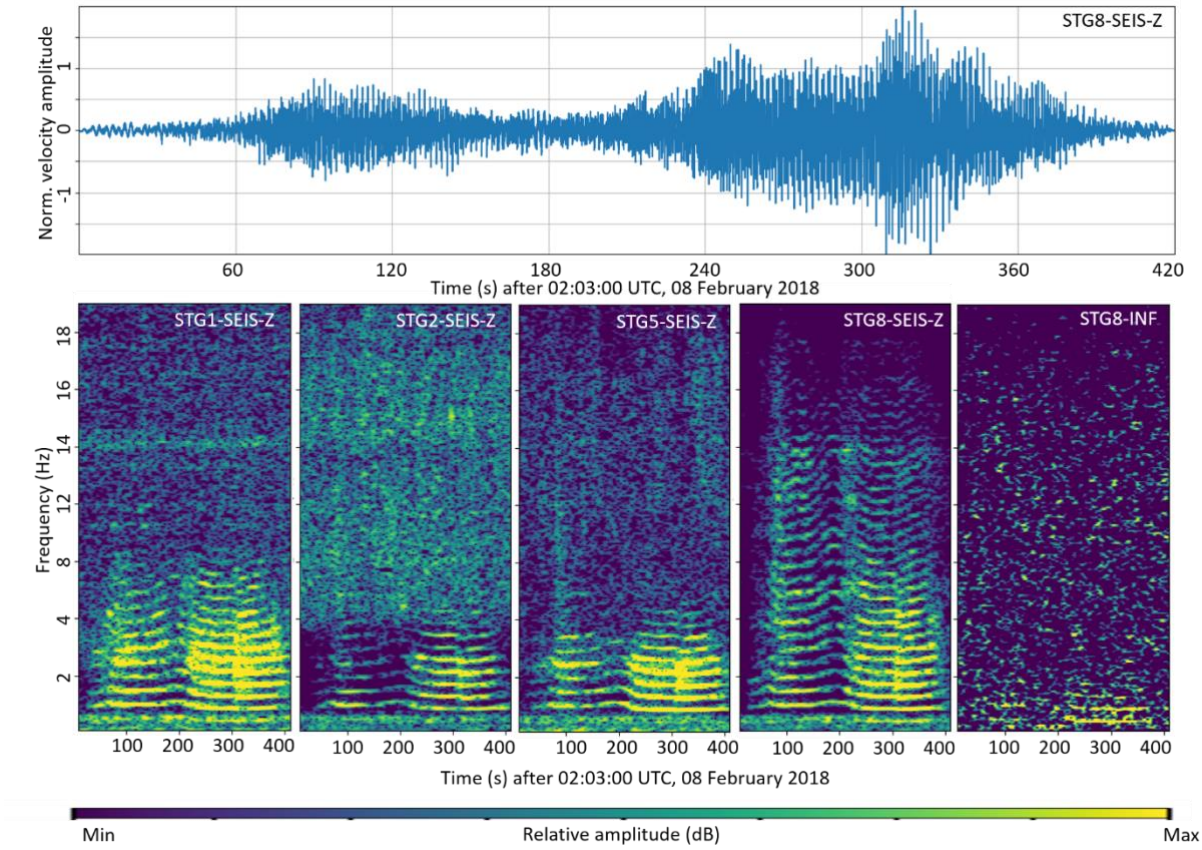

Figure 8. (a) Vertical (Z) velocity seismogram recorded on 08 February 2018 (02:03 UTC-02:10 UTC) at station STG8 (at 2.2 km from the active vent Caliente). The data have been bandpass filtered between 0.1 and 15 Hz. (b-f) Spectrograms computed from vertical velocity seismograms for same event as in panel a, at stations (b) STG1 (4.5 km), (c) STG2 (6.3 km), (d) STG5 (7.5 km), (e) STG8 (2.2 km), and (f) infrasound data at station STG8. The tremor signal is composed of distinct frequencies. The fundamental frequency (f_0) amounts to 0.5 Hz and shows upward and downward gliding. Up to 28 evenly spaced harmonics can be found at station STG8. The fundamental frequency and the first two harmonics can even be detected in the infrasound signal.

Figure 9 shows a tremor signal that occurred on 21 February 2018. Here, the tremor signal consisted of two clearly distinguishable bursts. The first burst started about 10 s after the beginning of the record shown and reached a low peak amplitude, which then decreased gradually. The second burst started after ~45 s and exhibited a marked increase in amplitude over about 30 s, before decreasing in amplitude over a period of ~6 minutes. The fundamental frequency f_0 observed in the spectrograms (Figure 9 bottom) of this tremor was 0.8 Hz, and momentarily reduced to 0.65 Hz between ~30 and 150 s. Up to 30 evenly spaced harmonics were determined at station STG8 while at stations STG1, STG2, and STG5, harmonics above 6 Hz were less energetic. The first three harmonics were visible in the infrasound recording for the first 150 s.

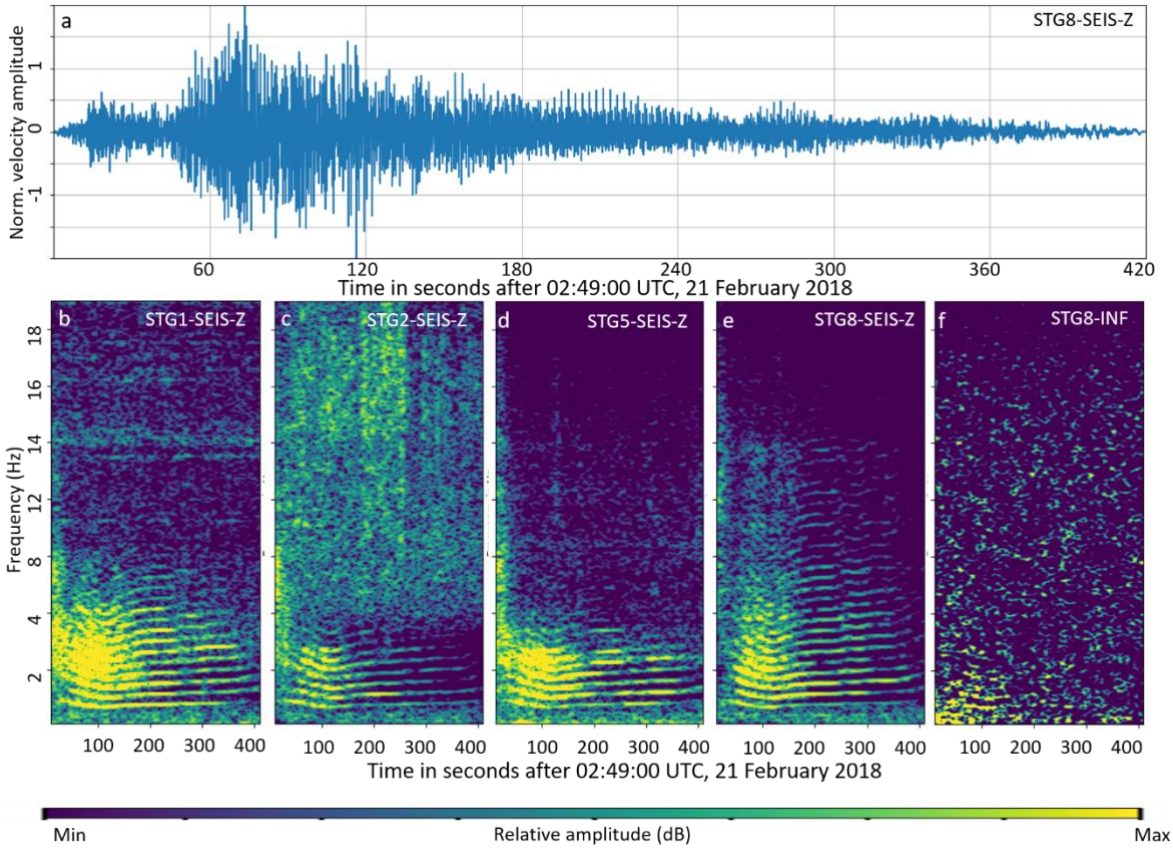

Figure 9. (a) Vertical (Z) velocity seismogram recorded on 21 February 2018 (02:49 UTC-02:56 UTC) at station STG8 (at 2.2 km from the active vent Caliente). (b-f) Spectrograms computed from vertical velocity seismograms for same event as in panel a, at stations (b) STG1 (4.5 km), (c) STG2 (6.3 km), (d) STG5 (7.5 km), (e) STG8 (2.2 km), and (f) infrasound data at station STG8. The fundamental frequency (f_0) amounts to 0.8 Hz and shows gliding. Up to 30 evenly spaced harmonics can be found at station STG8. The fundamental frequency and the first two harmonics can even be detected in the infrasound signal.

Figure 10 shows a complex explosion followed by tremor, monitored by thermography and seismicity. The thermographic data revealed that the emission of hot material was initiated with a low-amplitude seismic precursor, 2 s before arrival of the main explosion-type signal (marked by an abrupt increase in amplitude); arrival of the main seismic signal coincided with temperature increase associated with an emitted plume (Figure 10c). As the explosion signal amplitude waned, the seismic signals showed the overprint by tremor activity (blue to red transition on Fig. 10a); the tremor persisted in bursts and emission ensued with a considerable volume of hot material. The seismic signal was followed by tremor starting around 06:47 UTC. Unfortunately, clouds then obscured the volcanic activity in the final phase of seismicity. Yet, the thermographic data indicated that volcanic emissions persisted despite the reduction in seismic amplitude, suggesting gas emissions can outlast seismicity

in the detectable amplitude range (for closest station STG8). This event is analyzed in further detail in section 4.5.2

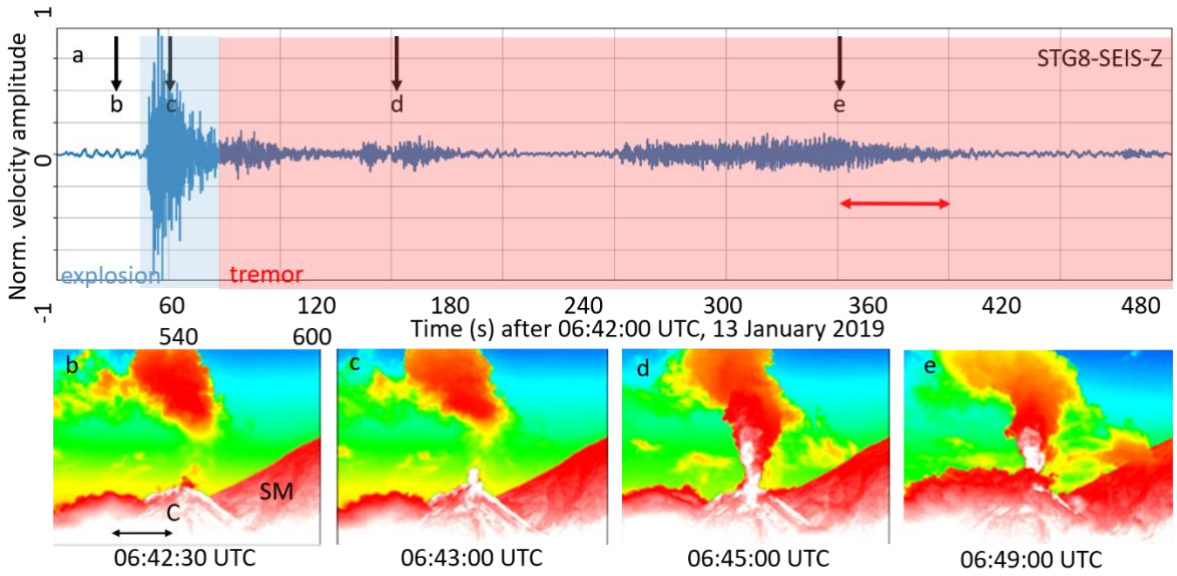

Figure 10. (a) Velocity seismogram recorded on 13 January 2019 (06:42 UTC-06:52 UTC) at station STG8 (at 2.2 km from the active vent Caliente), vertical component. The data have been bandpass filtered between 0.1 and 15 Hz. An explosion signal at 06:42:49 UTC is preceded by a low-amplitude precursor 2 s before the main explosion signal (blue box) and closely followed by a tremor sequence (pink box), which starts around 06:47 UTC. The red horizontal arrow marks the time for which amplitude spectra are shown in Figure 12. (b-e) Thermographic images recorded from (b) STG5 before the explosion (06:42:30 UTC), (c) simultaneously with the seismic explosion signal (06:43:00 UTC), (d) during low seismic amplitude (06:45:03 UTC) and (e) during the seismic recording of the tremor event (06:49:00 UTC), where clouds start to cover the dome of Caliente. The times are marked with black arrows in (a). C and SM (in panel b) mark Caliente and Santa Maria, respectively. The length of the arrow in panel b) corresponds to approximately 300 m at Caliente summit. White colors indicate the relatively warm regions, blue colors indicate relatively cold regions.

Compilation of the tremor data in 2018 indicated that the fundamental harmonic of those events (at frequency f_0) ranged between 0.2 and 0.8 Hz (Figure 11). Note that tremor events lasting more than 100 s were represented by consecutive data points in Figure 11 to account for frequency gliding (shown in Figures 8 and 9), as the fundamental frequency f_0 commonly evolved during a single tremor event. In these cases, consecutive data points in Figure 11 appear at increasing/ decreasing frequencies.

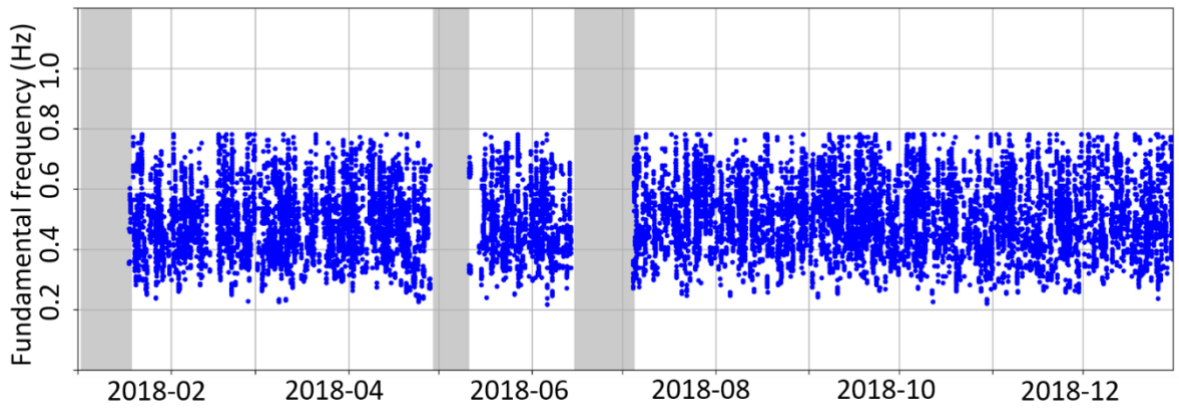

Figure 11: Fundamental frequencies f_0 computed for all harmonic tremor events during 2018 for time windows of 36 s each. The fundamental frequencies observed are entirely found in a frequency band between 0.2 Hz and 0.8 Hz. Tremor events that last longer than 100 s are presented by multiple, consecutive data points.

During the study period we observed variable numbers of harmonic tremor events. [Here we note that the detection of tremor was not ubiquitous at all stations; for instance, in 2018 we detected 1523 harmonic tremor events in the records of station STG8, but only 838 and 823 events at stations STG2 and STG5, respectively. Hence, we imposed the presence of harmonic tremor signals in the STG8 data as a criterion for the identification of all tremor.] During January 2019-March 2020, the average weekly occurrence of tremors was lower (10-40 events/week) than in 2018 (20-50 events/week) and since April 2020 (25-45 events/week. A similar distinction between these periods can be seen in the total average duration of tremor events which initially fluctuated between 40 and 130 minutes/week in 2018, 20-90 minutes per week in January 2019-March 2020, and 50-100 minutes per week after April 2020. Contrasting tremor durations in these periods suggests that the recurrence rate changed during the 33 months investigated.

4.5.2 Tremor depth estimation

Here we further our analysis of tremor signals by resolving their source depth. Our dataset allowed us to estimate the source depth of harmonic tremor signals by examining the decay of harmonics' amplitudes. We analyzed the amplitude decay of the harmonics with distance from the active crater for an event on 13 January 2020, 06:42:49 UTC-06:42:50 UTC (time indicated by red arrow in Figure 10). Amplitude spectra have been computed for stations LIN1-3, STG1, STG2, STG5 and STG8 and are shown in Figure 12. The fundamental frequency f_0 of this harmonic tremor signal is 0.405 Hz, whilst higher harmonics are clearly present in the spectra. The lowest panel shows a stacked amplitude spectrum computed

from the trace normalized spectra at stations STG8 and LIN3, and at least 24 harmonics were clearly distinguished.

The amplitude A of the second harmonic ($2 \cdot f_0$) at each station was used to compute amplitude decay for different source depths (equation 1) z between 0 and 8000 m below the crater. Figure 13a shows the regression determined for a source depth z = 500 m for all stations (solid line); in contrast, the dashed-line regression determined for the same depth, but with all stations apart from station STG8, as this station is deployed close to a dry river bed, which systematically lowered the spectral amplitudes. The misfit of the regression is determined, considering all stations (solid curve) or all stations excluding STG8 (dash curve); the minimum of the misfit function is regarded as most probable source depth (Figure 13b). Here, both misfit functions have their smallest value for source depths z around or below 500-750 m, thus constraining tremor origin.

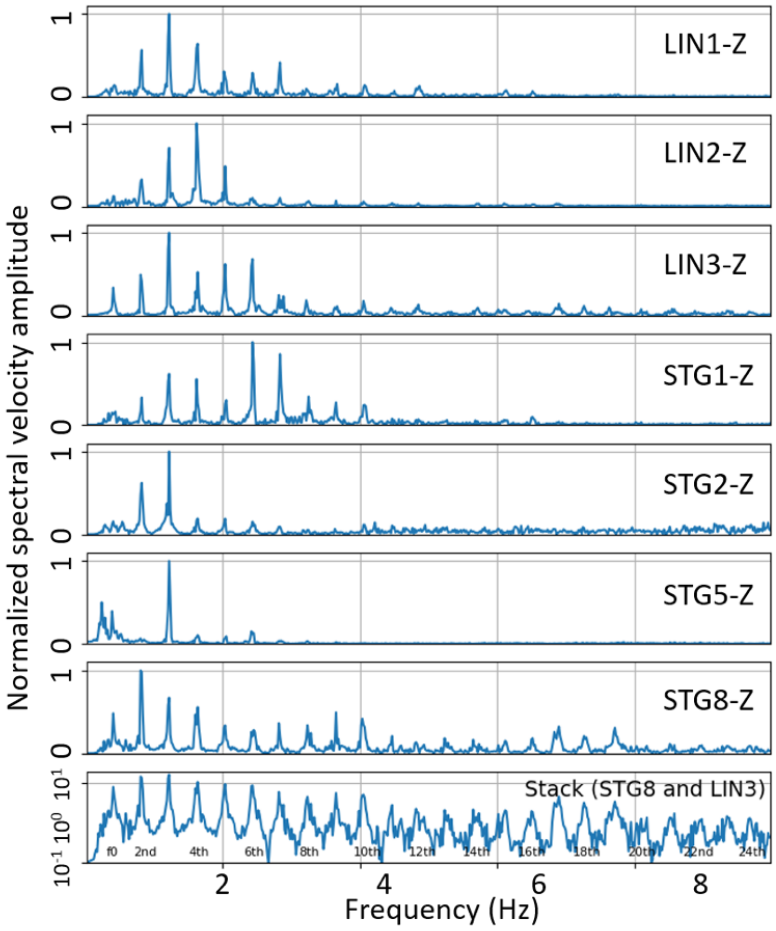

Figure 12. Normalized amplitude spectra computed for vertical velocity seismograms on January 13, 06:49 UTC-06:50 UTC (the period from which the spectra were computed is marked by a red arrow on Figure 10). LIN1-LIN3 were stations temporarily deployed in January 2019 at 3.9 km, 2.6 km and 0.5 km from the active vent Caliente. STG1 (4.5 km), STG2 (6.3 km), STG5 (7.5 km), and STG8 (2.2. km) are our four long-term stations. The data have been restituted using their instrument response function and highpass filtered at 0.25 Hz in order to suppress low frequency noise. The fundamental frequency

of the tremor signal amounts to 0.405 Hz and higher harmonics are visible at all stations. The lower panel displays the stacked spectrum computed from individually normalized spectra at the two closest stations STG8 and LIN3, highlighting over 24 harmonics (where even harmonics have been labelled).

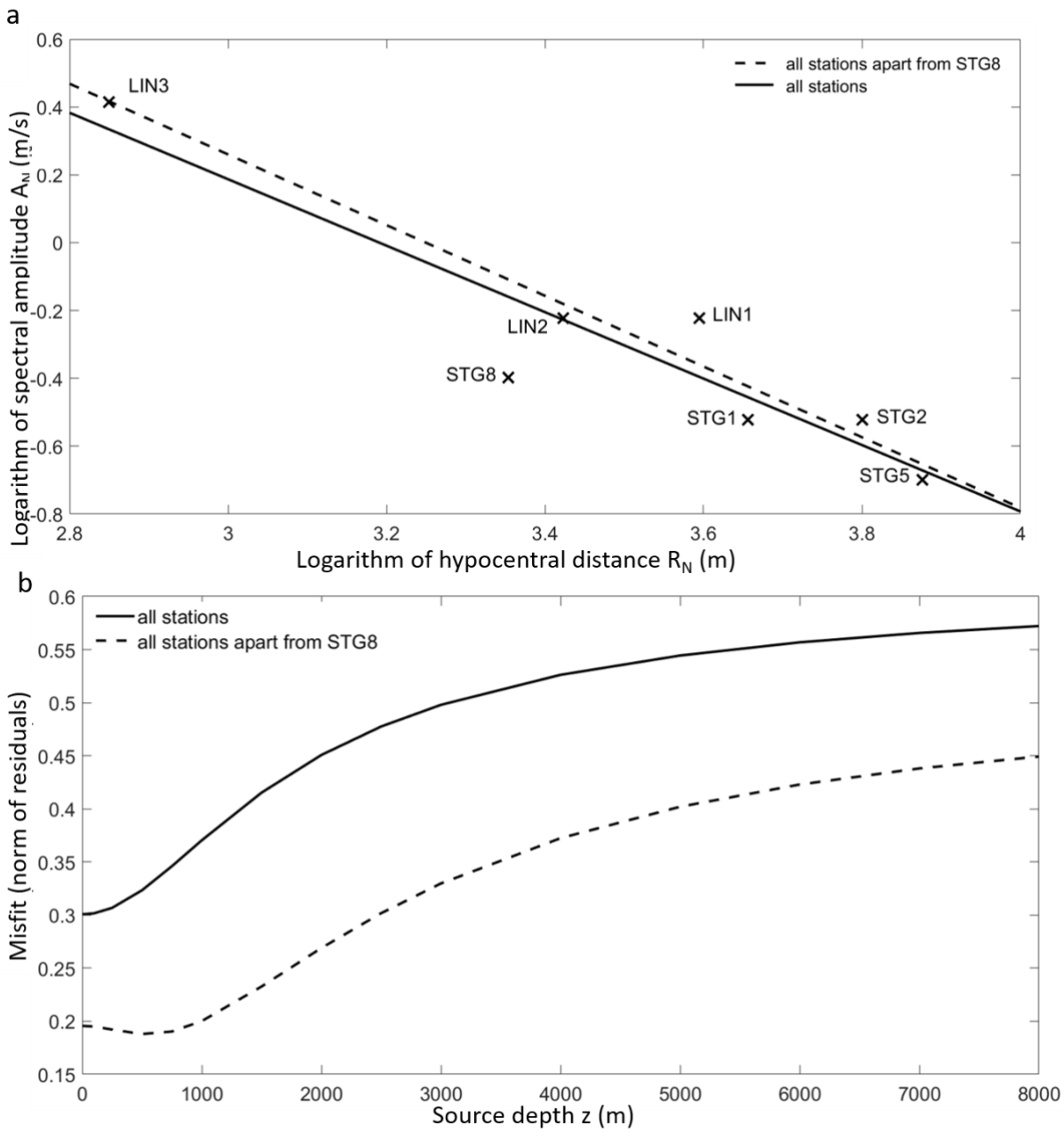

Figure 13. Tremor depth analysis. (a) Logarithm of spectral amplitudes A_N for the second harmonic for N stations (as displayed in Figure 12). For the determination of the hypocentral distance R_N, the source depth was 500 m in this Figure. The solid line shows the regression of the function $\log A_N(R_N) = \log A_0 - n \log R_N$ for all stations while the dashed line shows the regression for all stations but STG8 (as it shows relatively low amplitudes due to proximity to a river bed). (b) Misfits of the functions computed as norm of the residuals for different source depths z between 0 and 8000 m. The solid line shows the misfit function for all stations, whereas the dashed line shows a smaller misfit when excluding STG8. The smallest misfit values are resolved for source depths below or around 500-750 m, irrespective of the choice of stations.

5 Interpretation and Discussion

The observations made from our long-term, multiparametric instrument deployment allow us to get a better understanding of the range and level of volcanic activity, and of the potential source processes taking place at Santiaguito. Below we focus our interpretation and discussion on the seismic signals associated with volcanic activity at Santiaguito, and assess how the level of unrest varied over the course of our prolonged monitoring campaign

5.1 Volcano tectonic earthquakes

We recorded 129 individual VT earthquakes between January and April 2018. VTs are commonly inferred to result from brittle failure of sub-volcanic environments and have previously been attributed to wallrock faulting associated with, for instances, magma transport and creation of a magmatic conduit (Neuberg, 2000; Smith and Kilburn, 2010; Chouet and Mantoza, 2013). The VTs detected at Santiaguito were able to be identified on the seismic traces at several (minimum three) distal stations, which gave us the opportunity to locate hypocenters. Ten VTs were constrained to originate at depths between 1.3 and 2.3 km, approximately 1.5 km south-west of Caliente. This location is not coincidental as it sits along the regional NE-SW Zunil fault zone that links Santiaguito to Santa Maria (including the direction of sector collapse) and Volcán Cerro Quemado (to the NW of Santa Maria; Escobar-Wolf et al., 2010; Bennati et al., 2011); yet, before inferring any links between the recent VTs and regional faults, we turn to previous observations of such seismic signals. The occurrence of a volcano tectonic earthquake swarms at Santiaguito was, to our knowledge, reported for the first time by Lamb et al. (2019), who observed 275 VT earthquakes (from their station LB03 equivalent to our proximal station STG8) during an 11-hour period on 24 July 2016 (the hypocentral location was however not analyzed). VT events were recorded at this station until August 2016, which marked the end of the highly-explosive paroxysmal phase 2 (July 2015 – September 2016) and transition to renewed dome growth (phase 3). We found no swarms of VT earthquakes in the 2018-2020 period, nor did Lamb et al. (2019) during the dominantly effusive phase 3 in late 2016-2017, which may reflect the presence of an active (open) conduit associated with the ongoing dome growth. Thus, it may be that the 2015-2016 paroxysmal activity caused fracture damage around the Caliente magmatic conduit, which could have extended along the Zunil feeder fault zone in 2018.

5.2 Explosion seismic signals

Between January 2018 and September 2020, we recorded 70-100 explosions weekly. The above averages starkly contrast with the 300~500 weekly explosions that took place in the early 2015 dome growth phase that preceded the paroxysmal activity in July 2015 – September 2016 (Lamb et al., 2019; Carter et al., 2020). If the cause and mechanism of explosions remained the same in January 2018 – September 2020 as they were in early 2015, then the large difference in explosion recurrence rates between the two periods may provide us with information about the magmatic conditions.

Multiple studies suggest that the explosions are influenced by the presence of a relatively dense magma plug within the crater of Caliente (e.g., Bluth and Rose, 2004; Sahetapy-Engel et al., 2008). The momentary development of high strain rates near the conduit margins during magma ascent has been suggested to locally promote the brittle rupture of an otherwise ductile magma (during periods of, or in areas of, lower strain rates; Hornby et al., 2019a). Holland et al. (2011) suggested that explosions are the result of a sudden decompression of stored gas due to incremental movement of this plug during rupture events. The faint precursory signals which we observed 2-4 s before the seismic explosion signal might be related to opening of fractures upon shear near the conduit margin (e.g., Hornby et al., 2019a), before the whole magma column starts to slip (e.g., Lavallée et al., 2015). The fact that the explosion seismic signals were short in comparison to gas emissions observed on the thermographic images could be interpreted as a relatively fast crack opening with subsequent gas escape. This might continue as long as the crack remains open or until the tapped gas reservoir is discharged, which lends itself to a period of quiescence and volcanic edifice repose between explosions (e.g., Johnson et al., 2014; Lavallée et al., 2015). So, differences in explosion recurrence rates between early 2015 and 2018-2019 may be caused by different ascent rate conditions (e.g., Bain et al., 2019) combined with different recurrence rates of high gas fluxes (e.g., Michaut et al., 2013), possibly resulting from contrasting volatile concentration at the source in each period, and/ or permeability of the shallow magmatic conduit (e.g., Edmonds et al., 2003; Edmonds and Herd, 2007). Faster magma ascent rate (e.g., Bain et al., in review) and longer repose time between periods of high volatile fluxes associated with explosions would favor magma densification (e.g., Ashwell et al., 2015; Kennedy et al., 2016), fracture closure (Lamur et al., 2017) and enhance the likelihood (and thus degree) of fracture healing (Lamur et al., 2019); thus overall, the permeability of the shallow magma would have been lower, essentially plugging the upper conduit. Indeed, the 2018-2019 eruptive phase has been characterized by faster extrusion rates than those observed in 2014-2015, which may corroborate this interpretation of observed explosion recurrence rates in recent years.

Beyond the eruptive constraints afforded by explosion seismicity, conditions in the subsurface may also be inferred. We observed that the seismic signals associated with explosions are closely followed by an acoustic wave at co-located infrasound stations, which helped us approximate velocity in the subsurface. The explosion signals have previously been constrained to occur at a depth of ~300 m (Johnson et al., 2014); at station STG5, 7.5 km from Caliente, we can reasonably assume that the source of seismicity and acoustic signals are equally distant. With this assumption, and considering typical atmosphere sound velocities of 330-340 m/s, we used the 20-s arrival time difference between both signals to approximate seismic velocity V_p of the shallow subsurface between 3.0-3.5 km/s.

5.3 Eastern flank activity

Flank activity was characterized by variably emergent seismic signals, which occurred concurrently with the emission of hot plumes, commonly on the eastern flank of Caliente whenever thermal observations were available. Although active lava domes overspilling crater walls are common sites of rockfalls (e.g., Rose, 1972; Mueller et al., 2013), here we found subtle nuances which prevented us from ascertaining rockfalls as the origin of flank activity. Some of the events observed (e.g., Figure 7) showed more impulsive onset than the typical seismic signatures from rockfalls, lahars or pyroclastic density currents, as described by Lamb et al. (2019). The seismic signals of rockfalls described by Lamb et al. (2019) are marked by emergent onsets and decays with a slowly increasing and decreasing amplitude, so that their shape resembles a cigar. Our signals exhibit slightly sharper onset and longer duration than those observed by Lamb et al. (2019). We propose that the flank-activity-seismic signals with the sharpest onsets may have indicated a process with a more sudden start, such as a rupture in the edifice associated with prolonged fumarolic activity or large surficial breakoff leading to rockfalls. The subsequent release of hot material visible in the thermographic images may support this speculation, as the signals could stem from crack openings leading to prolonged fumarolic activity along the flank of Caliente or from sudden large-scale brecciation of the lava flow front descending the eastern flank. Zorn et al. (2020) constrained the lava flow velocities at approximately 15 m per day in February 2019. Flow front break-ups associated with upwelling of hot gases were witnessed during that particular (and other) field campaigns, but in our analysis of the signals of these events, we found that the seismic signals displayed lower amplitudes than, for instance, that described in Figure 7. Whilst it is very likely that the signals of flank activity were caused by rockfalls of variable sizes, it may be that other processes also took place; good visual observations will be required to examine these signals further in future multi-parametric studies.

5.4 Tremor signals

In January 2018 – September 2020 the monitoring record indicated extensive tremor activity with characteristic harmonics in the seismic and acoustic datasets. Tremor activity has previously been observed at Santiaguito; for instance, Johnson et al. (2009) also recorded volcanic tremor signals in seismic and infrasound datasets. They described harmonic tremors with a fundamental frequency f_0 of 0.43 Hz and approximately 10 well-defined harmonics; in the 1523 harmonic tremor sequences analyzed for 2018 we found fundamental frequencies f_0 in the range between 0.2 and 0.8 Hz and up to 30 harmonics. A key difference between our observations and previous ones is that Johnson et al. (2009) occasionally observed signals preceding explosive events and used this observation to associate tremor to increased gas emission ahead of an explosion. Here, we observed no tremor before, only directly or briefly (a few minutes) after an explosion.

The observation of harmonic tremor in the seismic and acoustic datasets suggests that the signal signature (i.e., harmonics) at the source is transferred to the atmosphere upon emission and may indicate a relatively shallow source connected to the atmosphere via fractures. A similar interpretation has been reached by Johnson et al. (2009) for tremor at Santiaguito, as well as at the active Sangay (Ecuador) and Karymsky (Russia) volcanoes, where the term “chugging events” was introduced to describe the flow of compressed gas in fractures (Lees and Ruiz, 2008; Lees et al., 2004; Johnson and Lees, 2000). Even though Scharff et al. (2014) did not observe tremor signals in their Doppler radar study they suggested that their fault-related explosion model could explain syn-eruption tremor signals, invoking free oscillation of the magmatic column when gas escapes through peripheral fractures near the conduit margin, causing local variations in friction, as described by the wagging model of Jellinek and Bercovici (2011). However, the difference in timescale and depth between our long-lasting seismic tremor and the 3 s long explosions originating at shallow depth (e.g., Scharff et al., 2014) demands further appraisal. Some studies have advanced that any kind of repeated movement in close succession could cause the generation of periodic waves. Neuberg et al. (2000) and Powell and Neuberg (2003) reproduced volcanic tremor at Soufrière Hills volcano (Montserrat) by superposition of long-period events at regular intervals. Hotovec et al. (2013) introduced a model in which closely repeating earthquakes, generated via stick-slip motion, created a periodic signal. Dmitrieva et al. (2013) evaluated the viability and implications of this tremor mechanism by introducing a frictional-faulting model, as Iverson et al. (2006) and Kendrick et al. (2014) showed that repetitive volcanic seismicity (drumbeat) can be caused by stick-slip motion of active faults in conduits; however, Powell and Neuberg (2003) indicated that the triggering mechanism and

879 timing of each sub-event need to be very stable and constant in order to generate harmonic
880 signals. Hotovec at el. (2013) analyzed the stability of their harmonic signals by numerically
881 increasing the error in periodicity of the Dirac comb signal. They observed that an increased
882 error degrades the harmonic nature of the signal and decreases the number of harmonics. In
883 both models (i.e., that of Neuberg et al. (2000) and Powell and Neuberg (2003) vs. that of
884 Hotovec et al. (2013) and Dmitrieva et al. (2013)), the fundamental frequency of the signal
885 showed strong and continuous up-gliding and preceded explosive events. Our signals,
886 however, showed up- and down-gliding of the fundamental frequency with less pronounced
887 amplitude, and followed explosive events. Thus, we advance that none of these rhythmic
888 seismicity models adequately explain our tremor observations, and it might be that fracture
889 outgassing and closure (due to gas depressurization; Lamur et al., 2017) as the dome settles
890 following an explosion (indicated by negative tilt; Lavallée et al., 2015), better explains the
891 occurrence of tremor at Santiaguito. In this case, the source of tremor must be associated
892 with the point at which gas is subjected to volume changes when exposed to lower pressures
893 in fractures.
894
895 We estimated the source depth of harmonic tremor signals to originate at, or above, a depth
896 of 1000 m, via the assumption that the geometrical amplitude decay is inversely proportional
897 to the distance (i.e., $\propto 1/R$). Although this approach is simplistic and the estimate from the
898 best fit is widely ranging, we believe that this depth estimate agrees well with the
899 observations that harmonic tremor signals are contemporaneous with a continuous discharge
900 of hot material (for those we observed), even after conclusion of the explosion seismic signal;
901 this would be feasible by the existence of opened fractures following explosions. Johnson et
902 al. (2009) reported diminished spectral amplitudes for the 2nd and 4th harmonics in the
903 tremor data, which they take as indication for a nonlinear excitation from fluid flow (*cf*. Julian
904 et al., 1994); an observation we cannot confirm from our data and analysis herein. It should
905 be noted that the model of Julian et al. (1994) was developed for low-viscosity magma
906 exhibiting laminar flow, which may not necessarily lead to similar observations if one
907 considers turbulence during fluid flow in fractures and high viscosities, as constrained for the
908 shallow magma at Santiaguito (e.g., Avard and Whittington, 2012). Our long-term
909 observations of small to moderate gas-and-ash explosive activity and tremor events provided
910 an excellent database to further the analysis of volcano-seismic signals in future studies.
911
912 **5.5 Protracted activity at Santiaguito lava dome**
913
914 The analysis afforded by the long-term monitored datasets provide a view into the steadiness
915 or the occurrence of shifts in activity and behavior (Figure 2), not resolvable with short

monitoring campaigns. Here we noted that the recurrence rate of explosions remains relatively steady during January 2018 – September 2020; yet, scrutinizing the dataset in 2018-2019, we observed slight fluctuations in explosion rates. The periods with slightly higher activity (e.g., April and October 2018, and March 2019, do not coincide with the height of the rainy or dry seasons (which characterize the tropical climate of Guatemala), so, we conclude that this variation likely reflected subtle fluctuations in the level of volcanic unrest, which we propose ought to be examined over longer timeframe. In comparison, the occurrence and duration of tremor showed no variations in ~6-months period, but activity appeared to be slightly lower during January 2019 - March 2020 than in the rest of the study period (although we are missing ~4 months of data to more robustly support this observation).

At Santiaguito, gas-and-ash explosions as well as gas emission events share a close relationship with faults and fractures in the lava dome (e.g., Johnson et al., 2008; Scharff et al., 2014; Lavallée et al., 2015; Hornby et al., 2019), accumulated over the course of regular inflation-deflation cycles (e.g., Johnson et al., 2014), faulting events and cataclasis (e.g., Hornby et al., 2019b), and explosions (e.g., Carter et al., 2020). Additionally, our observations point to a strong synergy between explosions and gas emissions, as tremors generally accompany and follow explosions. Magma ascent and eruptive cyclicity are commonly linked to gas flux (e.g., Michaut et al., 2013), hence one may expect that variations in recurrence rates would be comparable in both types of signals; yet, we observed contrasting periodicity for the explosions versus tremor, although these are only faintly defined. The cause for such differences may rest in the way in which pore pressure develops and accumulates in the magmatic column: whilst harmonic tremor likely reflects gas flow in fractures, explosions represent a complex pressure accumulation in both fractures and the vesicular network of the magmatic column; thus, we surmise that whilst their occurrence may be related, they represent different manifestations of physical and mechanical controls. We advance that future studies should examine the relationships between explosions and harmonic tremor resulting from vigorous gas emissions further to identify the degree of fluid pressure accumulation in shallow magmatic conduits. The observation of subtle variations in activity at Santiaguito in periods of 6 months or longer, points to the importance of integrating long-term, multiparametric field campaigns to resolve relationships between magmatism, structural development and volcanic activity.

6 Summary

Analysis of seismic and infrasound data recorded during January 2018-September 2020 at Santiaguito lava dome complex reveals a variety of signals and activity. The data were classified using automated search algorithms and correlated with Caliente's surface activity via thermographic imagery and visual observations.

Seismic signals from both regional tectonic earthquakes and volcano tectonic earthquakes were found in the dataset. Overall, we identified between ~70 and 250 earthquake events/week (not associated to explosions) and observed that the number of earthquakes was slightly higher during January and October of 2018 than during the rest of the study period. We have identified 129 volcano-tectonic earthquakes in January-April 2018, of which ten were constrained to originate at source depths between 1.3-2.3 km, 1.5 km southwest of Caliente, likely located along the regional Zunil fault. The data contained seismic signals with variably emergent onsets, concomitant with lofting of hot plumes visible above the flank of the dome in the thermographic imagery, likely resulting from rockfalls along the flanks of Caliente. The seismic analysis revealed the occurrence of signals associated with gas-and-ash explosions from the dome surface (these were confirmed by thermal, visual and infrasound data). The signals of explosions typically showed an impulsive onset and their amplitude decayed rapidly within 60-90 s. Low-amplitude signals occasionally preceded explosions by 2-4 s. Overall, we identified, on average, around ~70-100 weekly explosions. Finally, we observed harmonic tremor signals in the seismic, and occasionally acoustic, data with fundamental frequencies between 0.2 and 0.8 Hz, and up to 30 harmonics. Harmonic tremor signals were observed directly after (up to a few minutes) explosions, and whenever thermographic images were available we observed gas emissions from the central vent during their occurrence. Harmonic tremor persisted for up to 20 minutes and showed clear evidence of frequency gliding (up and down). Using the spectral amplitude decay of the first harmonic with distance we estimated the source depth of harmonic tremor at shallow depths, about 500-750 m below the crater. The monitored dataset indicated that tremor recurrence rate and duration where slightly lower and shorter, respectively, in January 2019-March 2020, than in the rest of the investigated period. Together, the frequency of explosions and harmonic tremor showed slight variations during the study period; the former showed a slight periodicity of ~6 months whereas the latter showed no clear periodicity. Differences in occurrence rate may reflect the different conduit regions in which volatiles accumulate; tremor signals are associated with gas flow in fractures, whereas explosions are associated with gas accumulation in both magma vesicles and fractures. We advance that the long-term multiparametric dataset presented in this study provides a strong baseline to resolve long-term volcanic behavior and elaborate more sophisticated eruption and signal source models at Santiaguito.

Acknowledgments

We are ever so grateful to Armando Pineda for his help with field work and station maintenance. This study was funded by the Geophysical Institute at KIT and through an urgency grant of the Natural Environment Research Council on “Rapid deployment of a multi-parameter geophysical experiment at Santiaguito volcano, Guatemala following a marked increase in explosive activity” (Grant NE/P007708/1). This research was further supported by a Starting Grant from the European Research Council (ERC) to Y. Lavallée on Strain Localisation in Magma (SLiM, no. 306488), an Early Career Fellowship of the Leverhulme Trust granted to J.E. Kendrick (ECF-2016-325) and Research Fellowship of the Leverhulme Trust granted to Y. Lavallée (RF-2019-526\4). We also acknowledge and thank Diana Roman and an anonymous reviewer for their constructive comments and suggestions, which greatly helped to improve the manuscript.

References

Aki, K., Fehler, M. and Das, S., 1977. Source mechanism of volcanic tremor: fluid-driven crack models and their application to the 1963 Kilauea eruption. J. Volcanol. Geotherm. Res., 2, 259-287.

Andrews, B.J., 2014. Magmatic storage conditions, decompression rate, and incipient caldera collapse of the 1902 eruption of Santa Maria Volcano, Guatemala. J. Volcanol. Geotherm. Res. 282, 103–114. doi: 10.1016/j.jvolgeores.2014.06.009

Ashwell, P.A., Kendrick J.E., Lavallée Y., Kennedy B.M., Hess K.U., von Aulock F.W., Wadsworth F.B., Vasseur J., Dingwell D.B., 2015. Permeability of compacting porous lavas. J. Geophys. Res., Solid Earth 120 (3) :1605-1622.

Avard, G. and Whittington, A.G., 2012. Rheology of arc dacite lavas: experimental determination at low strain rates. Bulletin of Volcanology 74, 1039-1056.

Bain, A.A., Lamur A., Kendrick J.E., Lavallée Y., Calder E.S., Cortes J.A., Cortes G.P., 2019. Constraints on the porosity, permeability and porous micro-structure of highly-crystalline andesitic magma during plug formation. J. Volcanol. Geotherm. Res. 379, 72-89.

Bain, A.A., Kendrick, J.E., Lamur, A., Lavallée, Y., Calder, E.S., Cortés, J.A., Cortés, G.P., Martinez, D.G. and Torres, R.A., in review. Micro-textural controls on magma rheology and Vulcanian explosion cyclicity. Frontiers in Earth Science.

Bennati, L., Finizola, A., Walker, J.A., Lopez, D.L., Higuera-Diaz, I.C., Schütze, C., Barahona, F., Cartagena, R., Conde, V., Funes, R., Rios, C., 2011. Fluid circulation in a complex volcano-tectonic setting, inferred from self-potential and soil CO_2 flux surveys: the Santa María–Cerro Quemado–Zunil volcanoes and Xela caldera (Northwestern Guatemala). J. Volcanol. Geotherm. Res. 199, 216–229. doi: 10.1016/j.jvolgeores.2010.11.008

Benoit, J.P. and McNutt, S.R., 1997. New constraints on source processes of volcanic tremor at Arenal Volcano, Costa Rica, using broadband seismic data. Geophys. Res. Lett. 24, 449-452.

Bluth, G.J. and Rose, W.I., 2004. Observations of eruptive activity at Santiaguito volcano, Guatemala. J. Volcanol. Geotherm. Res. 136, 297-302. doi:10.1016/j.jvolgeores.2004.06.001

Burbach, G.V., Frohlich, C., Pennington, W.D. and Matumoto, T., 1984. Seismicity and tectonics of the subducted Cocos Plate. J. Geophys. Res., 89, 7719– 7735. doi:10.1029/JB089iB09p07719

Carter, W., Rietbrock, A., Lavallée, Y., Gottschämmer, E., Díaz Moreno, A., Kendrick, J.E., Lamb, O.D., Wallace, P. A., Chigna, G., De Angelis, S., 2020. Statistical evidence of transitioning open-vent activity towards a paroxysmal period at Volcán Santiaguito (Guatemala) during 2014–2018. J. Volcanol. Geotherm. Res., 398. doi.org/10.1016/j.jvolgeores.2020.106891

Chouet, B.A. and Matoza, R.S., 2013. A multi-decadal view of seismic methods for detecting precursors of magma movement and eruption. J. Volcanol. Geotherm. Res., 252.

De Angelis, S., Lamb, O.D., Lamur, A., Hornby, A.J., von Aulock, F. W., Chigna, G., Lavallée, Y. and Rietbrock, A., 2016. Characterization of moderate ash-and-gas explosions at Santiaguito volcano, Guatemala, from infrasound waveform inversion and thermal infrared. Geophys. Res. Lett., 43, 6220-6227. doi:10.1002/2016GL069098

Delle Donne, D. and Ripepe, M., 2012. High-frame rate thermal imagery of Strombolian explosions: implications for explosive and infrasonic source dynamics. J. Geophys. Res., 117. doi:10.1029/2011JB008987

Dmitrieva, K., Hotovec-Ellis, A.J., Prejean, S. and Dunham, E.M., 2013. Frictional-faulting model for harmonic tremor before Redoubt Volcano eruptions. Nature Geosci., 6, 652–656. doi:10.1038/NGEO1879

Ebmeier, S.K., Biggs, J., Mather, T.A., Elliott, J.R., Wadge, G. and Amelung, F., 2012. Measuring large topographic change with InSAR: lava thicknesses, extrusion rate and subsidence rate at Santiaguito volcano, Guatemala. Earth Planet. Sci. Lett. 335-336, 216-225.

Edmonds, M. and Herd, R.A., 2007. A volcanic degassing event at the explosive-effusive transition. Geophys. Res. Lett. 34 (21).

Edmonds, M., Oppenheimer, C., Pyle, D.M., Herd R.A. and Thompson, G., 2003. SO2 emissions from Soufriere Hills Volcano and their relationship to conduit permeability, hydrothermal interaction and degassing regime. J. Volcanol. Geotherm. Res. 124 (1-2), 23-43.

Escobar-Wolf, R., Gomez, R.O. and Rose, W.I., 2010. Geologic Map of Santiaguito Volcano, Guatemala. Geological Society of America Digital Map and Chart Series 8.

Global Volcanism Program, 2016. Report on Santa Maria (Guatemala). In: Venzke, E. (Ed.), Bulletin of the Global Volcanism Network, 41:9. Smithsonian Institution.

Green, D. and Neuberg, J., 2006. Waveform classification of volcanic low-frequency earthquake swarms and its implication at Soufrière Hills Volcano, Montserrat. J. Volcanol. Geotherm. Res. 153, 51–63.

Harris, A.J.L., Rose, W.I. and Flynn, L.P., 2003. Temporal trends in lava dome extrusion at Santiaguito 1922 - 2000. Bull. Volcanol. 65, 77-89. doi:10.1007/s00445-002-0243-0

Hellweg, M., 2000. Physical models for the source of Lascar's harmonic tremor. J. Volcanol. Geotherm. Res. 101, 183-198.

Holland, A.S.P., Watson, I.M., Phillips, J.C., Caricchi, L. and Dalton, M.P., 2011. Degassing processes during lava dome growth: Insights from Santiaguito lava dome, Guatemala. J. Volcanol. Geotherm. Res., 202, 153-166.

Hornby, A.J., Lavallée, Y., Kendrick, J.E., De Angelis, S., Lamur, A., Lamb, O., Rietbrock, A. and Chigna, G., 2019a. Brittle-Ductile Deformation and Tensile Rupture of Dome Lava During Inflation at Santiaguito, Guatemala. J. Geophys. Res., 124, 10, 107–10, 131. doi.org/10.1029/2018JB017253

1080 Hornby, A.J., Lavallée, Y., Kendrick, J.E., Rollinson, G., Butcher, A., Kueppers, U., Cimarelli,
1081 C., Clesham, S., Chigna G., 2019b. Phase partitioning during fragmentation revealed by
1082 QEMSCAN particle mineralogical analysis of volcanic ash. Nature Scientific Reports 9: 126.

1083 Hotovec, A., Prejean, S.G., Vidale, J.E. and Gomberg, J., 2013. Strongly gliding harmonic
1084 tremor during the 2009 eruption of Redoubt Volcano. J. Volcanol. Geotherm. Res., 259, 89-
1085 99. doi:10.1016/j.jvolgeores.2012.01.001

1086 INSIVUMEH, 2019. Located earthquake catalog 2018 and 2019 by Geophysics Department
1087 of Instituto Nacional de Sismología, Vulcanología, Meteorología e Hidrología, INSIVUMEH,
1088 using the National Seismic Network in Guatemala (FDSN code: GI) www.insivumeh.gob.gt

1089 Iverson, R., Dzurisin, D., Gardner, C., Gerlach, T.M., LaHusen, R.G., Lisowski, M., Major,
1090 J.J., Malone, S.D., Messerich, J.A., Moran, S.C., Pallister, J.S., Qamar, A. I., Schilling, S.P.
1091 and Vallance, J.W., 2006. Dynamics of seismogenic volcanic extrusion at Mount St Helens in
1092 2004–05. Nature, 444, 439–443. doi.org/10.1038/nature05322

1093 Jellinek, A. and Bercovici, D., 2011. Seismic tremors and magma wagging during explosive
1094 volcanism. Nature 470, 522–525. doi:10.1038/nature09828

1095 Johnson, J.B. and Lees, J.M., 2000. Plugs and chugs—seismic and acoustic observations of
1096 degassing explosions at Karymsky, Russia and Sangay, Ecuador. J. Volcanol. Geotherm.
1097 Res., 101, 67-82.

1098 Johnson, J.B., Harris, A.J.L., Sahetapy-Engel, S.T.M., Wolf, R. and Rose, W.I., 2004.
1099 Explosion dynamics of pyroclastic eruptions at Santiaguito Volcano. Geophys. Res. Lett., 31,
1100 L06610. doi:10.1029/2003GL019079

1101 Johnson, J.B., Lees, J.M., Gerst, A., Sahagian, D.L. and Varley, N.R., 2008. Long-period
1102 earthquakes and co-eruptive dome inflation seen with particle image velocimetry. Nature,
1103 456, 377-381.

1104 Johnson, J.B., Sanderson, R., Lyons, J., Escobar-Wolf, R., Waite, G. and Lees, J.M., 2009.
1105 Dissection of a composite volcanic earthquake at Santiaguito, Guatemala. Geophys. Res.
1106 Lett., 36, L16308. doi:10.1029/2009GL039370

1107 Johnson, J.B., Lees, J.M. and Varley, N.R., 2011. Characterizing complex eruptive activity at
1108 Santiaguito, Guatemala using infrasound semblance in networked arrays. J. Volcanol.
1109 Geotherm. Res., 199, 1-14.

1110 Johnson, J.B., Lyons, J.J., Andrews, B.J. and Lees, J.M., 2014. Explosive dome eruptions
1111 modulated by periodic gas-driven inflation. Geophys. Res. Lett. 41, 6689–6697.

1112 Jones, K.R. and Johnson, J.B., 2011. Mapping complex vent eruptive activity at Santiaguito,
1113 Guatemala using network infrasound semblance. J. Volcanol. Geotherm. Res., 199, 15-24.

1114 Julian, B.R., 1994. Volcanic tremor: Nonlinear excitation by fluid flow, J. Geophys. Res., 99,
1115 11859-11877. doi:10.1029/93JB03129

1116 Kendrick, J.E., Lavallée, Y., Hirose,T., Di Toro, G., Hornby, A.J., De Angelis, S. and
1117 Dingwell, D.B., 2014. Volcanic drumbeat seismicity caused by stick-slip motion and
1118 magmatic frictional melting. Nature Geosci., 7**,** 438–442. doi.org/10.1038/ngeo2146

1119 Kennedy, B.M., Wadsworth F.B., Schipper C.I., Jellinek A.M., Vasseur J., von Aulock F.W.,
1120 Hess K.-U., Russell J.K., Lavallée Y., Nichols A.R.L. and Dingwell D.B., 2016. Surface
1121 tension driven processes densify and retain permeability in magma and lava. Earth and
1122 Planetary Science Letters 433, 116-124.

1123 Konstantinou, K. and Schlindwein, V., 2002. Nature, wavefield properties and source
1124 mechanism of volcanic tremor: a review. J. Volcanol. Geotherm. Res. 119, 161- 187.
1125 doi:10.1016/S0377- 0273(02)00311-6

1126 Lamb, O.D., Lamur, A., Díaz Moreno, A., De Angelis, S., Hornby, A.J., von Aulock, F.W.,
1127 Kendrick, J.E., Wallace, P.A., Gottschämmer, E., Rietbrock, A., Alvarez, I., Chigna, G. and
1128 Lavallée, Y., 2019. Disruption of Long-Term Effusive-Explosive Activity at Santiaguito,
1129 Guatemala. Front. Earth Sci. 6:253. doi:10.3389/feart.2018.00253

1130 Lamur, A., Kendrick, J.E., Eggertsson, G.H., Wall, R.J., Ashworth, J.D., Lavallée, Y., 2017.
1131 The permeability of fractured rocks in pressurised volcanic and geothermal systems. Nature
1132 Sci. Rep., 7, 6173. doi:10.1038/s41598-017-05460-4

1133 Lamur, A., Kendrick, J.E., Wadsworth, F.B. and Lavallée, Y., 2019. Fracture healing and
1134 strength recovery in magmatic liquids. Geology 47(3):195-198.

1135 Lavallée, Y., Benson, P.M., Heap, M., Hess, K.-U., Flaws, A. and Dingwell, D.B., 2013.
1136 Reconstructing magma failure and the degassing network of dome-building eruptions.
1137 Geology 41, 515-518.

1138 Lavallée, Y., Dingwell, D., Johnson, J., Cimarelli, C., Hornby, A.J., von Aulock, F.W.,
1139 Kennedy, B.M., Andrews, B. J., Wadsworth, F.B., Rhodes, E. and Chigna, G., 2015. Thermal
1140 vesiculation during volcanic eruptions. Nature, 528, 544–547, doi:10.1038/nature16153.

1141 Lees, J.M. and Ruiz, M., 2008. Non-linear explosion tremor at Sangay, Volcano, Ecuador, J.
1142 Volcanol. Geotherm. Res., 176, 170-178.

1143 Lees, J.M., Gordeev, E. and Ripepe, M., 2004. Explosions and periodic tremor at Karymsky
1144 volcano, Kamchatka, Russia, *Geophys. J. Int.*, 158. doi:10.1111/j.1365-246X.2004.02239.x

1145 Lesage, P., Mora, M.M., Alvarado G.E., Pacheco J. and Métaxian J.-P., 2006. Complex
1146 behavior and source model of the tremor at Arenal volcano, Costa Rica. J. Volcanol.
1147 Geotherm. Res., 157, 49-59.

1148 McNutt, S.R. and Roman, D.C., 2015. Volcanic Seismicity. In: Sigurdsson, H. (Ed.), The
1149 Encyclopedia of Volcanoes, Second Edition, Elsevier Inc., London, San Diego, Waltham,
1150 Oxford.

1151 Michaut, C., Ricard, Y., Bercovici, D., Sparks, R.S.J., 2013. Eruption cyclicity at silicic
1152 volcanoes potentially caused by magmatic gas waves. Nature Geosci., 6, 856–860.
1153 doi:org/10.1038/ngeo1928

1154 Mueller, S.B., Varley, N.R., Küppers, U., Lesage, P., Reyes Davila, G.Á. and Dingwell, D.B.,
1155 2013. Quantification of magma ascent rate through rockfall monitoring at the
1156 growing/collapsing lava dome of Volcán de Colima, Mexico, Solid Earth 4:201-203.
1157 doi:10.5194/se-4-201-2013

1158 Nadeau, P.A., Palma, J.L. and Waite, G. P., 2011. Linking volcanic tremor, degassing, and
1159 eruption dynamics via SO_2 imaging, Geophys. Res. Lett., 38, 1. Doi: 10.1029/2010GL045820

1160 Neuberg, J., 2000. Characteristics and causes of shallow seismicity in andesite volcanoes.
1161 Philos. Trans. R. Soc. London, A 358, 1533 – 1546.

1162 Neuberg, J., Luckett, R., Baptie, B. and Olsen, K.B., 2000. Models of tremor and low-
1163 frequency earthquake swarms on Montserrat. J. Volcanol. Geotherm. Res., 101, 83-104.
1164 doi:10.1016/S0377-0273(00)00169-4

1165 Powell, T.W. and Neuberg, J., 2003. Time dependent features in tremor spectra. J. Volcanol.
1166 Geotherm. Res., 128, 177-185.

Rhodes, E., Kennedy, B.M., Lavallée, Y., Hornby, A., Edwards, M. and Chigna, G., 2018. Textural insights into the evolving lava dome cycles at Santiaguito Lava Dome, Guatemala. Front. Earth Sci. 6:30. doi:10.3389/feart.2018.00030

Ripepe, M., 1996. Evidence for gas influence on volcanic signals recorded at Stromboli. J. Volcanol. Geotherm. Res. 70, 221-233.

Ripepe, M., Poggi, P., Braun, T. and Gordeev, E., 1996. Infra-sonic waves and volcanic tremor at Stromboli. Geophys. Res. Lett. 23, 181-184.

Roman, D.C., 2017. Automated detection and characterization of harmonic tremor in continuous seismic data, Geophys. Res. Lett., 44, 6065-6073, doi:10.1002/2017GL073715

Rose, W.I., 1972. Santiaguito Volcanic Dome, Guatemala, Geological Society of America Bulletin 83,1413-1434.

Rose, W.I., 1973. Pattern and mechanism of volcanic activity at the Santiaguito volcanic dome, Guatemala. Bull. Volcanol., 37: 73. doi:10.1007/BF02596881

Rose, W.I., 1987. Volcanic activity at Santiaguito volcano, 1976–1984. In: Fink, J.H., (Ed.), The emplacement of silicic domes and lava flows. Geol.Soc. Am., Special Paper 212, 17–28.

Rose, W.I., Pearson, T. and Bonis, S., 1976. Nuée Ardente Eruption from the Foot of a Dacite Lava Flow, Santiaguito Volcano, Guatemala. Bull. Volcanol., 40:23. doi:10.1007/BF02599827

Sahetapy-Engel, S.T., Harris, A.J.L. and Marchetti, E., 2008. Thermal, seismic and infrasound observations of persistent explosive activity and conduit dynamics at Santiaguito lava dome, Guatemala. J. Volcanol. Geotherm. Res., 173, 1-14.

Salvage, R. and Neuberg, J., 2016. Using a cross correlation technique to refine the accuracy of the failure forecast method: application to Soufrière Hills volcano, Montserrat. J. Volcanol. Geotherm. Res. 324, 118–133.

Sanderson, R.W., Johnson, J.B. and Lees, J. M., 2010. Ultra-long period seismic signals and cyclic deflation coincident with eruptions at Santiaguito. J. Volcanol. Geotherm. Res., 198, 35-44. doi:10.1016/j.jvolgeores.2010.08.007

Scharff, L., Ziemen, F., Hort, M., Gerst, A. and Johnson, J.B., 2012. A detailed view into the eruption clouds of Santiaguito volcano, Guatemala, using Doppler radar. J. Geophys. Res., 117, B04201. doi:10.1029/2011JB008542

Scharff, L., Hort, M. and Gerst, A., 2014. The dynamics of the dome at Santiaguito volcano, Guatemala. Geophys. J. Int., 197, 926-942. doi:10.1093/gji/ggu069

Schlindwein, V., Wassermann, J. and Scherbaum, F., 1995. Spectral analysis of harmonic tremor signals at Mt. Semeru volcano, Indonesia. Geophys. Res. Lett., 22, 1685-1688.

Scott, J.A.J., 2013. The Santiaguito volcanic dome complex, Guatemala. https://vhub.org/resources/2268, last accessed 10 November 2020.

Seidl, D., Schick, R. and Riuscetti, M., 1981. Volcanic tremors at Etna: a model for hydraulic origin. Bull. Volcanol. 44: 43-56.

Smith, R. and Kilburn, C.R.J., 2010. Forecasting eruptions after long repose intervals from accelerating rates of rock fracture: The June 1991 eruption of Mount Pinatubo, Philippines. J. Volcanol. Geotherm. Res. 191, 129-136. doi.org/10.1016/j.jvolgeores.2010.01.006

Spieler, O., Kennedy, B., Kueppers, U., Dingwell, D.B., Scheu, B. and Taddeucci, J., 2004. The fragmentation threshold of pyroclastic rocks. Earth Planet. Sci. Lett. 226(1–2):139–148.

Wallace, P.A., Lamb, O.D., De Angelis, S., Kendrick, J.E., Hornby, A.J., Díaz Moreno, A., von Aulock, F.W., González, P.J., Lamur, A., Utley, J.E.P., Rietbrock, A., Chigna, G. and Lavallée, A., 2020. Integrated constraints on explosive eruption intensification at Santiaguito dome complex, Guatemala. Earth Planet. Sci. Lett., 536.

Zorn, E.U., Walter, T.R., Johnson, J.B., Mania, R., 2020. UAS-based tracking of the Santiaguito Lava Dome, Guatemala. Sci Rep, 10**,** 8644. doi.org/10.1038/s41598-020-65386-2